Bioconjugation studies of an EGF-R targeting ligand on dendronized iron oxide nanoparticles to target head and neck cancer cells

Barbara Freis, María De Los Ángeles Ramírez, Sonia Furgiuele, Fabrice Journe, Clémence Cheignon, Loïc J. Charbonnière, Céline Henoumont, Celine Kiefer, Damien Mertz, Christine Affolter-Zbaraszczuk, Florent Meyer, Sven Saussez, Sophie Laurent, Mariana Tasso, Sylvie Bégin-Colin

PII: S0378-5173(23)00074-1
DOI: https://doi.org/10.1016/j.ijpharm.2023.122654
Reference: IJP 122654

To appear in: *International Journal of Pharmaceutics*

Received Date: 31 July 2022
Revised Date: 20 January 2023
Accepted Date: 23 January 2023

Please cite this article as: B. Freis, M. De Los Ángeles Ramírez, S. Furgiuele, F. Journe, C. Cheignon, L.J. Charbonnière, C. Henoumont, C. Kiefer, D. Mertz, C. Affolter-Zbaraszczuk, F. Meyer, S. Saussez, S. Laurent, M. Tasso, S. Bégin-Colin, Bioconjugation studies of an EGF-R targeting ligand on dendronized iron oxide nanoparticles to target head and neck cancer cells, *International Journal of Pharmaceutics* (2023), doi: https://doi.org/10.1016/j.ijpharm.2023.122654

Bioconjugation studies of an EGF-R targeting ligand on dendronized iron oxide nanoparticles to target head and neck cancer cells

Barbara Freis[1,2], María De Los Ángeles Ramírez[1], Sonia Furgiuele[3], Fabrice Journe[3], Clémence Cheignon[4], Loïc J. Charbonnière[4], Céline Henoumont[2], Celine Kiefer[1], Damien Mertz[1], Christine Affolter-Zbaraszczuk[5], Florent Meyer[5], Sven Saussez[3], Sophie Laurent[2*], Mariana Tasso[1,6], Sylvie Bégin-Colin[1*]

(1) Université de Strasbourg, CNRS, Institut de Physique et Chimie des Matériaux, UMR CNRS-UdS 7504, 23 Rue du Loess, BP 43, 67034 Strasbourg, France.

(2) Laboratoire de NMR et d'imagerie moléculaire, Université de Mons, Avenue Maistriau 19, 7000 Mons, Belgium.

(3) Department of Human Anatomy and Experimental Oncology, Faculty of Medicine, Research Institute for Health Sciences and Technology, University of Mons (UMONS), Avenue du Champ de Mars, 8, 7000 Mons, Belgium.

(4) Université de Strasbourg, CNRS, Institut Pluridisciplinaire Hubert Curien, UMR 7178, 25, rue Becquerel, 67087 Strasbourg, France.

(5) Inserm U1121, Centre de recherche en biomédecine de Strasbourg, 1 rue Eugène Boeckel, CS 60026, 67084 Strasbourg Cedex, France.

(6) Instituto de Investigaciones Fisicoquímicas Teóricas y Aplicadas (INIFTA), Departamento de Química, Facultad de Ciencias Exactas, Universidad Nacional de La Plata - CONICET, Diagonal 113 y 64, 1900 La Plata, Argentina.

Abstract

A major challenge in nanomedicine is designing nanoplatforms (NPFs) to selectively target abnormal cells to ensure early diagnosis and targeted therapy. Among developed NPFs, iron oxide nanoparticles (IONPs) are good MRI contrast agents and can be used for therapy by hyperthermia and as radio-sensitizing agents. Active targeting is a promising method for selective IONPs accumulation in cancer tissues and is generally performed by using targeting ligands (TL). Here, a TL specific for the epidermal growth factor receptor (EGFR) is bound to the surface of dendronized IONPs to produce nanostructures able to specifically recognize EGFR-positive FaDu and 93-Vu head and neck cancer cell lines. Several parameters were optimized to ensure a high coupling yield and to adequately quantify the amount of TL per nanoparticle. Nanostructures with variable amounts of TL on the surface were produced and evaluated for their potential to specifically target and be thereafter internalized by cells. Compared to the bare NPs, the presence of the TL at the surface was shown to be effective to enhance their internalization and to play a role in the total amount of iron present per cell.

1. Introduction

In nanomedicine, two main mechanisms are reported for the uptake of theranostic NPFs in tumor sites. These mechanisms are known as “passive targeting” and “active targeting”. Briefly, passive targeting occurs because the NPFs, due to their size, can pass easily through the abnormal vasculature of tumors, which generally present irregular fenestrations and poor lymphatic drainage compared to healthy tissues[1–3]. Through this process, certain NPFs tend to accumulate in the tumor site. This mechanism was proposed in the 1980s under the name of Enhanced Permeability and Retention (EPR) effect [4]. Diagnostic and therapy procedures relying on the EPR effect are markedly susceptible to the tumor microenvironment and to the effective capacity of the NPFs to accumulate in the target areas in high amounts. Active targeting offers then the possibility to site-direct the NPFs to the areas of interest, thereby enhancing their local concentration.

Therefore, a lot of research was done in order to develop active targeting. The purpose of such active targeting mechanism is also to selectively reach abnormal tissues and to treat only them, avoiding the unwanted accumulation of nanoparticles in healthy tissues. In this sense, the active targeting consists firstly in finding a cell receptor overexpressed in the type of cancer of interest[2,3,5–8]. Once the suitable overexpressed receptor is defined, a specific molecule, often named targeting ligand (TL) selected to interact with the cell receptor, can be used to deliver the nanoparticles directly to this site. Among the most used receptors are, e.g., the folate receptor, which can be targeted with folic acid on the surface of NPFs[9]; or the Human Epidermal Growth Factor Receptor 2 (HER2+), which is recognized by the monoclonal antibody Trastuzumab[10]. Peptides, nano-bodies, affibodies, proteins, small organic molecules or nucleic acids[2,3,7,11–14] constitute examples of short TL. The large antibodies or the smaller versions of them, the fragment antigen-binding (Fabs), are also common TL[15].

These targeting ligands are generally coupled to drugs or at the surface of functionalized nanoparticles. Iron oxide nanoparticles (IONPs) are among the most developed and promising NPFs at the moment for their use as contrast agent for magnetic resonance imaging (MRI) and for hyperthermia therapies.[2,3,5–8,16,17]. Without TL, they usually accumulate in tumors via intratumoral injection or by passive targeting as a result of the EPR effect. Another way to increase their local accumulation is to perform a magnetic targeting, in which a magnetic field gradient guides IONPs towards the tumor. The main drawback of this technique is the requirement of a magnet that should be easily positioned near the tumor, thus limiting this strategy to specific cases. Active targeting studies have been also conducted but *Wilhem et. al.*~~, after reviewing the literature from the previous 10 years,~~ observed that just 0.7% (median) of the administered nanoparticle dose (with or without TL) was found to be delivered to solid tumors after reviewing the literature from the previous 10 years[17]. Similar low percentages of internalized IONPs were reported also by *Alphandery*[16]. Developing NPFs able to specifically target diseased organs and tissues without their prompt removal from circulation and further accumulation in the reticulo endothelial system remains a challenge. Among the characteristics that can be tuned in IONPs to ensure a high and specific accumulation, one can mention the kind of the organic coating, the size and nature of the TL, its hydrophobicity/hydrophilicity balance, the final mean hydrodynamic size and the surface charge, as the most relevant. In our case, we have developed IONPs with a mean diameter of 10 nm coated with polyethylene glycol (PEG)-based dendron molecules (dendronized IONPs: DNPs), which were demonstrated in several *in vitro* and *in vivo* studies to ensure antifouling properties to DNPs [18–26]. Thus, these DNPs, which display a favourable *in vivo* biodistribution and bioelimination profile, are well adapted for further investigating affinity targeting. Coupled to a melanin TL, DNPs were shown to selectively target melanin granules or hypoxia states after i.v. injection[27,28]. Even if specific targeting was evidenced in these studies, the internalized amount in tumors remained low and the amount of TL was not optimized. Altogether, these DNPs displaying a particularly good biodistribution, without a significant uptake in healthy tissues and showing potential for active targeting, are useful NPFs to answer some important questions related to the targeting process.

The choice of the TL is challenging as it must target overexpressed receptors at the surface of cancer cells. Moreover, the size of the TL must be suitable compared to the mean size of IONPs. Furthermore, the NPF-immobilized TL needs to conserve its recognition capacity towards its target, a fact that imposes *sine qua non* conditions to the chosen bioconjugation approach to avoid the involvement of the active site in the coupling[29,30]. In the case of short TL, a major concern is to avoid abrupt changes in the 3D conformation of the molecule (upon conjugation to the NPFs) that may alter its interactions with the cellular receptors. Lastly, the TL must remain fully exposed at the surface of the IONPs and not buried inside the polymer ligand.

In this work, our aim is to target head and neck cancer (HNC) cells with functionalized DNPs. The chosen cancer model for this work was HNC, using the FaDu cell line derived from a hypopharyngeal carcinoma and the 93-VU line from an oral cavity carcinoma. Both cell lines have elevated levels of the EGFR.[31] This receptor, which belongs to the HER/ErbB family of receptors tyrosine kinases (RTKs), is overexpressed in 90% of head and neck squamous cell carcinoma (HNSCC)[32–34]. It has been demonstrated that EGFR has a strong role for tumorigenesis: the higher its expression, the more resistance to therapies and the poorer outcome for patients are evidenced[32]. Some therapies were developed to inhibit the EGFR with the use of anti-EGFR antibodies, like Cetuximab, which, up to now is the only approved targeted drug for HNSCC.[35] However, its efficacy remains limited due to the unresolved resistance mechanism of the tumor.[36] As an alternative to antibodies, peptides appear as a good substitute: they have high penetration into solid tumor tissues and limited immunogenic potential[37,38]. Additionally, peptides are small, simple to manufacture and easy to adapt to several bioconjugation approaches by the addition of specific amino acid residues, such as lysines, or terminal tags, such as the Histidine tag. During the conjugation on DNPs bearing peripheral carboxylate groups, the amount of peptide can be tuned to cover a desired surface of the DNPs. Peptides with small molecular weight and high EGFR affinity have been the focus of research for active targeting agents combined with drug delivery systems. The dodecapeptide GE11 (YHWYGYTPQNVI) has been shown to have good affinity for EGFR[39]. Many analogs of GE11 peptide were synthesized to test their binding affinity to triple negative breast cancer lines overexpressing EGFR. Among 29 of them, Hossein-Nejad-Ariani *et al*. demonstrated that the peptide analogue 22 (YHWYGYTPENVI) (P22) shows several fold higher uptake compared to the lead peptide GE11 when evaluated in solution and in *in vitro* assays[40]. This fact makes P22 an interesting candidate to target other types of cancers with overexpression of EGFR.

As the EGFR inhibition strategy was not efficient enough, the objective here is to specifically internalize DNPs bearing the TL P22 in HNC cell lines by taking advantage of their EGFR overexpression and to use the therapeutic properties of IONPs based on magnetic hyperthermia or photothermia[24,41,42]

There is a wide spectrum of bioconjugation reactions[43] used to attach TLs at the surface of functionalized IONPs; globally they can be divided into two types: covalent conjugations or non-covalent conjugations. The carbodiimide chemistry[44], Michael addition[45,46], click Chemistry[47–49], or Diels-Alder cycloaddition, among others, belong to the first group[3,50]. In non-covalent conjugation, the most common are carried out by electrostatic interactions, metal affinity coordination or biotin-avidin interaction[51]. As DNPs possess carboxylate functions at their periphery, the coupling of P22 on the DNP surface was achieved using carbodiimidation reactions between a free carboxylate group present at the extremity of the dendron molecules, and a primary amine of P22, resulting in the formation of an amide bond.

In this work, we have optimized the coupling reaction of P22 at the DNPs' surface and studied the impact of the coupling strategies on the amount of coupled TL and on cell internalisation. During these investigations, we confirmed the much acknowledged importance that should be conferred to the purity and storage conditions of the reagents involved in this reaction (particularly EDC and sulfo-NHS), as well as the significant impact of carefully controlling the pH during the different steps of the coupling.

We also dedicated efforts to validate the presence of the TL at the surface of IONPs and to quantify it. Commonly, the presence of TL at the surface of IONPs may be checked by FTIR spectroscopy or thermogravimetric analysis if the amount of TL is high enough, but most often, it is simply confirmed by the observation of an increase in the hydrodynamic size or a change in zeta potential values. The quantification of the amount of TL at the surface of IONPs rather than the determination of its presence or absence on it is a technically challenging step [2,6,13,52].This quantification can be done by an indirect way, analysing the amount of uncoupled TL, or directly by fluorescence spectroscopy, for example, when a fluorescent TL is used. The presence of the P22 at the surface of the DNPs was verified by zeta potential changes and by the increase in hydrodynamic size. The P22 coupled amount was quantified by an indirect method based on the quantification of the unbound peptide by HPLC-UV (between 40% and 50% coverage of dendrons). Finally, the specific internalization of these optimized DNPs bearing the P22 targeting ligand by the two HNC cell lines was studied and discussed in light of the total amount of peptide per NP. Compared to bare DNPs, the presence of P22 at the surface was shown to enhance the internalization by a factor 2 to 4 in the tested conditions when increasing the amount of grafted TL.

2. Experimental

2.1 Materials

Iron stearate ($FeSt_3$) was purchased from TCI (purity minimum 60% of stearic acid, 5.8 to 7% of iron and maximum 10% of free acid), $FeSt_2$ was home made. Acetone (purity 99.8%), chloroform (purity 99%) and THF (purity 99.5%) were purchased from Carlo Erba. Dioctyl ether (OE) (purity 99%), HEPES buffer (purity 99.5%), N-hydroxy sulfosuccinimide (sulfo-NHS, purity 98%), sodium carbonate (Na_2CO_3, purity 99,5%) and thiazolyl blue tetrazolium bromide (MTT, purity 98%) were purchased from Sigma Aldrich. Peptide 22 (P22) (purity 98.7%) was purchased from Polypeptide. Sodium hydrogen carbonate ($NaHCO_3$, purity 99.5%) was purchased from Bioreagent. 1-Ethyl-3-(3'-dimethylaminopropyl) carbodiimide hydrochloride (EDC-HCl, purity 99%) was purchased from Carl Roth. Oleic acid (OA, purity 99%) was purchased from Alfa Aesar. Dimethyl sulfoxide (DMSO, purity 99%) was purchased from Fisher Scientific. The dendron D1-2P was provided by Superbranche company. All reagents for cell culture: cell medium (DMEM (Dulbecco's Modified Eagle's Medium)) High Glucose (with Glutamine and Sodium Pyruvate), PBS 1X, Penicillin/Streptomycin 100X (P/S), trypsin-EDTA and Foetal Bovine Serum (FBS) were purchased from Dominique Dutscher. Cell lines FaDu and 93-VU were donated by the Department of Human Anatomy and Experimental Oncology from the University of Mons (FaDu provided from ATCC (ATCC® HTB43™) and 93VU~~-147T~~ from the University Medical Centre of Amsterdam (Dr. de Winter)).

2.2 Synthesis of 10 nm IONPs

Iron oxide nanoparticles were synthesized by thermal decomposition of an iron stearate precursor[53] in an organic solvent with a high boiling point and a surfactant[54–56]. 2.2 mmol of $FeSt_3$ (1.99 g) or $FeSt_2$ (1.44 g), 4.4 mmol of OA (1.24g) were mixed with OE (16.2 g, 20 mL) in a two-neck round-bottom-flask of 100 mL. The mixture was first heated to 120°C (heating device temperature: 130°C) for 60 min to dissolve the reagents in OE. The condenser was then connected to the flask and the mixture was heated up to 290°C (heating device temperature: 320°C) with a 5°C/min ramp. The mixture was refluxed at 290°C for 120 min. The obtained black NPs suspension was cooled down to 100°C to proceed to the washing steps.

2.3 Washing

10 mL of chloroform were added to the IONPs suspension at a temperature around 100°C and the suspension was introduced in a flask containing 400 mL of acetone. This mixture was heated at 60°C for 1 h under mechanical stirring using a thermal bath. The IONPs were collected with a magnet and the

supernatant was discarded. The collected IONPs were re-dispersed in 50 mL of chloroform. 400 mL of acetone were added again to proceed to a second washing step: the mixture was once more heated at 60°C for 45 min under mechanical stirring. At the end, the IONPs were collected with a magnet and the supernatant was discarded. Finally, the IONPs were re-suspended in 40 mL of THF for their storage or further utilization.

2.4 Dendronization of IONPs

The ligand exchange between OA and the dendron (D1-2P) was performed in THF[22]. Briefly, 5 mL of IONPs@OA at 1 mg Fe/mL were stirred for 24 h with 7 mg of dendron. To maximize the ligand exchange and remove most of oleic acid molecules[57], the suspension was then purified by ultrafiltration. 5 mg of dendron were added to the mixture for another 24 h of stirring. The suspension was mixed with hexane (volume ratio 1/3:2/3) to precipitate the DNPs. The suspension was centrifuged at 8000 rpm for 5 min and the supernatant was discarded. Finally, the DNPs were collected and dispersed in deionized water. The water suspension was purified by ultrafiltration 3 times.

2.5 Coupling reaction

The DNPs suspension was initially buffered-exchanged with HEPES 0.1 M, pH 6.5 in a centrifugal filter unit (Amicon®, MW cut off: 30 kDa; 10 min at 8000 rpm), the filtrate was suspended in the appropriate volume to reach a final concentration of 5 mg Fe/mL in HEPES. The suspension was thereafter mixed with EDC (20 molar excess compared to carboxylate groups present on dendron molecules) during 10 min and then sulfo-NHS (20 molar excess compared to carboxylate groups present on the dendron molecule) was added during additional 20 min. Upon the sulfo-NHS addition, the volume was increased to reach a final iron concentration of 0.5 mg/mL in HEPES buffer. The activated DNPs were rinsed with 0.1 M carbonate buffer, pH 9.2, in a centrifugal filter unit (10 min at 8000 rpm) to eliminate excess EDC, sulfo-NHS and other possible reaction intermediates. The filtrate was rapidly recovered and mixed with various P22 molar equivalents (compared to dendron molecule) in carbonate buffer. The volume of the reaction was completed with carbonate buffer to reach a final iron concentration of 0.5 mg/mL. The reaction was let overnight at room temperature under magnetic stirring. At the end, the supernatant was recovered by centrifugation (10 min at 8000 rpm) in centrifugal filter units. Three washes with milliQ water were done and the washes recovered for unbound P22 quantification.

2.6 Characterization techniques

2.6.1 TEM

The IONPs were characterized by transmission electron microscopy (TEM) with a JEOL 2100 microscope operating at 200 kV (point resolution 0.18 nm). The size distribution of NPs was estimated from the size measurements of more than 300 nanoparticles using ImageJ software.

2.6.2 X-Ray Diffraction

The X-ray diffraction (XRD) patterns were collected at room temperature with a Bruker D8 Discover diffractometer in Bragg Brentano geometry equipped with a monochromatic copper radiation source ($K\alpha 1 = 0.154056$ nm) and an energy resolved Lynx-Eye XE-T detector in the 25–65° (2θ) range with a scan step of 0.03°. High purity silicon powder ($a = 0.543082$ nm) was used as an internal standard.

The diffraction patterns were refined by LeBail's[58] method using the Fullprof software[59]. The background, modeled as a linear function based on 20 experimental points, was refined, as well as the zero shift. The peaks were modeled with the modified Thompson-Cox-Hasting (TCH) pseudo-Voigt profile function.

2.6.3 FTIR analysis

The ligand exchanged was confirmed with standard infrared spectra recorded between 4000 and 400 cm^{-1} with a Fourier Transform infrared (FTIR) spectrometer, Spectrum 100 from Perkin Elmer. Samples were ground and diluted in a non-absorbent KBr matrix before their analysis.

2.6.4 Dynamic Light Scattering and Zeta Potential

Dynamic Light Scattering measurements were performed on a MALVERN (nano ZetaSizer) equipment to assess the colloidal stability of the IONPs suspension in water and to determine their mean hydrodynamic diameter (D_h) after ligand exchange. The electrophoretic mobility was also recorded using the same equipment in order to obtain the zeta potential. ~~zeta potential was also recorded using the same equipment~~. The coupling of the TL was confirmed by an increase of D_h and a change in the zeta potential.

2.6.5 High Resolution Magic-Angle Spinning NMR (HRMAS NMR)

HRMAS NMR experiments were conducted on a Bruker FT-NMR Advance 500 equipped with an 11.75 T superconducting ultra-shield magnet. All the experiments were performed at a spinning rate of 5 kHz with a 50 µL zirconium rotor. This technique was used to confirm the presence of the TL at the surface of the IONPs.

2.6.6 Nuclear magnetic resonance dispersion (NMRD) profiles

Proton NMRD profiles were recorded using a Stelar Fast Field Cycling relaxometer (Mede, Italy). The system operates over a range of magnetic fields extending from 0.25 mT to 0.94 T (0.01–40 MHz) at 37 °C. T_1 and T_2 measurements were performed on a Bruker Minispec mq60 (Karlsruhe, Germany) working at a Larmor frequency of 60 MHz (1.41 T) at 37 °C.

2.6.7 High Performance Liquid Chromatography-UV spectroscopy (HPLC-UV)

HPLC-UV analysis was performed on an Agilent 1100 system equipped with a Diode-Array Detector (DAD). 10 µL of samples (supernatant and washes obtained after the coupling reaction for P22 quantification), were injected onto the column (Zorbax Extend-C18, 150 x 4.6 mm, 3.5 µm, Agilent) at room temperature. Ultrapure water, HPLC grade solvents and additives were used for the analysis. The elution gradient was carried out with trifluoroacetic acid (TFA) 0.1% (mobile phase A) and acetonitrile acidified with TFA 0.1% (mobile phase B) at a flow-rate of 1 mL/min. The mobile phase gradient was programmed with the following time course: 10% mobile phase B at 0 min, linear increase to 60% B at 15 min, held 1 min, linear decrease to 10% B at 17 min and held 7 min. The DAD was used as detector, with simultaneous detections at 220 ± 5 nm and 280 ± 5 nm. Quantification was realized by integration of the peak of the chromatogram corresponding to the analyte of interest compared to the integration calculated from a calibration curve of a standard solution of P22 (Figure S1).

2.7 Cell lines

FaDu (hypopharyngeal carcinoma) and 93-VU (oral cavity carcinoma) were cultured in DMEM medium supplemented with 10% FBS, 1% P/S and 2% L-Glutamine (200mM). They were cultured in an incubator at 37°C with 5% CO_2 under fully humidified conditions.

2.8 Cell viability assay

Cell viability assays were performed using the MTT [3-(4,5-dimethylthiazol-2-yl)-2,5-diphenyltetrazoliumbromide] assay. FaDu or 93-VU cells were seeded in 96 well plates at a density of 10^4 cells/well. After 24 h, the medium was taken out and DNPs in fresh medium were added at different concentrations (from 0 µg/mL to 400 µg/mL Fe) together with a negative control with 100 µL DMSO. The cells were grown for 24 h at 37 °C and 5% CO_2 to ~80% confluence. After 24 h the medium was retrieved, and the cells were washed twice with PBS and incubated with 100 µL of a MTT solution (0.5 mg/mL in cell medium). The plates were incubated for 3 h at 37°C and 5% CO_2, then the MTT solution was taken out and 100 µL of DMSO were added to each plate to dissolve the crystals under orbital shaking. The absorbance was read in a microplate reader (Xenius XC spectrophotometer (SAFAS, Monaco)) at 570 nm. The cytotoxicity was expressed as a percentage of cell viability compared to the control cells that were not exposed to the DNPs. The number of experiments for each condition was ≥ 3.

2.9 Iron uptake

The internalization study of DNPs and DNPs@P22 into cells at a concentration of 100 µg/mL was measured using the well-known Prussian Blue reaction developed by *Boutry et al*[60]. FaDu or 93-VU cells were seeded in a 6-well plate and incubated 24 h at 37 °C and 5% CO_2 for cells' attachment to reach 80% confluence in 24 hrs. The next day, the medium was replaced with fresh medium containing 100 µg/mL of DNPs or DNPs@P22 and the cells were left in the incubator for additional 24 h. Then, cells were trypsinized, recovered gently from the wells in a 1:2 volume ratio of trypsin to cell medium and then counted in a hemacytometer. After cell counting, cells were pelleted by centrifugation and washed three times with PBS. The final cell pellet was lysed with 5 N HCl for 24 h at 37°C. HCl also digested the cell-internalized DNPs leading to Fe^{3+}. The digested solution was finally put in contact with potassium ferrocyanide trihydrate, a salt which will react with Fe^{3+} to form a colored complex: the Prussian Blue dye. Furthermore, 100µL of suspension of DNPs at various concentrations were digested in the same conditions as the cell pellets to build a calibration curve (0 to 0.3 µmol/mL Fe). (Figure S1). All suspensions were let under orbital stirring for 15 min, and the absorbance was read in a microplate reader (Xenius XC spectrophotometer (SAFAS, Monaco)) at 630 nm. In this way, the amount of iron internalized per cell could be determined. The number of experiments for each condition was ≥ 3.

3. Results

3.1 Characterization of IONPs

IONPs were synthesized by the thermal decomposition method using a standard established protocol[54–56] and were characterized structurally. TEM images gave information on the shape and size distribution of IONPs (Figure 1 A), showing that they are spherical with a monomodal size distribution and a mean diameter of 12.8 ± 1.8 nm (Figure 1B). The X-Ray Diffraction pattern (Figure 1C) displays the characteristic XRD peaks of an iron oxide spinel structure. The lattice parameter calculated from this XRD pattern thanks to profile matching on FullProf (Figure S2) is of 8.37 Å, which is, as expected, intermediate between those of the magnetite and maghemite phases (8.395 Å and 8.347 Å, respectively)[54].

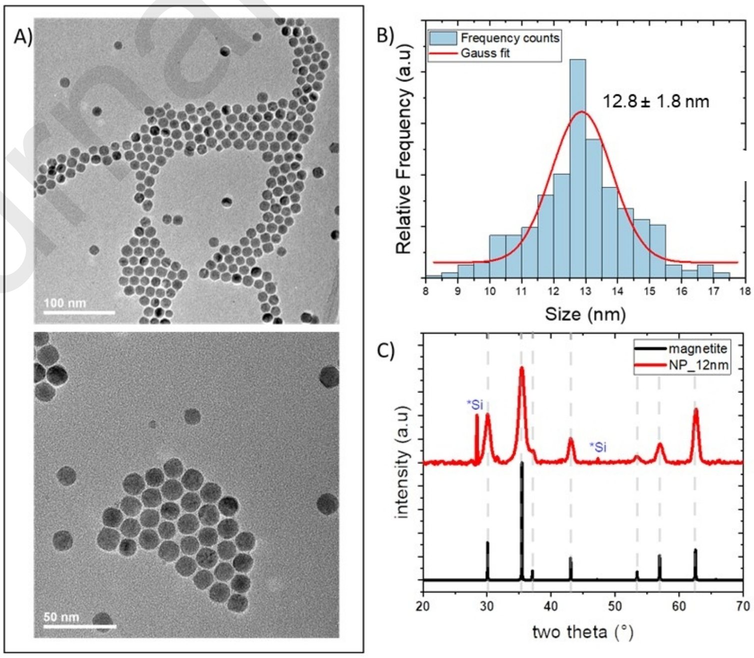

*Figure 1: A) TEM images of IONPs, B) Size distribution determined from TEM images and C) bulk magnetite and IONPs XRD pattern (*Si (silicon) is an internal reference).*

3.2 Coating of IONPs with dendron molecules (dendronization)

After the synthesis, IONPs remain coated with hydrophobic oleic acid ligands. Dendronization is thus an essential step to obtain stable colloidal suspensions of IONPs in water, this procedure occurs by a ligand exchange process (Figure 2.A).[22] The chemical formula of the dendron molecule is given in Figure 2.B: the dendron bears two phosphonate groups at one side for a strong anchoring of the dendron at the surface of IONPs[22,26,57] and three PEG chains at the opposite side with the central one being longer and ending with a carboxylate function. This free carboxylate group is used to couple the TL, fluorophores, or molecules of interest at the surface of DNPs.

FTIR analysis has confirmed the dendronization of IONPS. In Figure 2.C, the comparison of IR spectra of the dendron, of IONPs coated with oleic acid and of DNPs showed the presence, in the DNPs IR spectrum, of the bands of PEG (C-O-C bond) chains of dendron around 1100 cm^{-1} and a modification of the phosphonate bands in the wavenumber range 1100-800 cm^{-1} (proving the anchoring of dendrons through the phosphonate groups)[22]. This confirmed the efficacy of the ligand exchange process. The presence of the dendron and of the low remaining amount of oleic acid was also demonstrated by HRMAS as can be seen in Figure S3 showing HRMAS spectra of IONPs, DNPs and the dendron molecules. Indeed, the presence of two phosphonate groups used to anchor the dendron at the surface of IONPs has been shown effective to ensure a low amount of remaining oleic acid[57].

As the final objective is to use these DNPs in *in vitro* or *in vivo* studies, it is crucial to control this ligand exchange to preserve a good hydrodynamic size distribution with a mean hydrodynamic size smaller than 100 nm. The hydrodynamic size distribution after the dendronization step is assessed from ~~determined by~~ Dynamic Light Scattering (DLS) measurements and is monomodal with a mean hydrodynamic size of 18.7 nm (Figure 4.A). The surface density deduced from elemental analysis is of ~1.4 dendron/nm^2 in agreement with the expected value[61] which corresponds to ~700 dendron molecules per DNP.

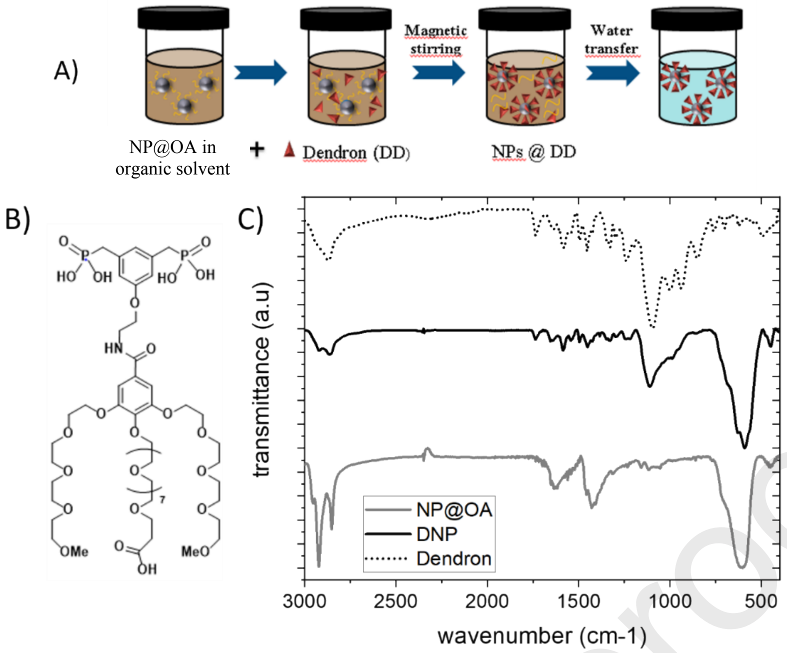

Figure 2 : A) Scheme of the ligand exchange process B) Scheme of the dendron molecule, C) FTIR spectra of the dendron (black doted spectrum), of IONPs coated with oleic acid (grey spectrum) and of DNPs (black spectrum).

3.3 Coupling reaction of TL on the peripheral carboxylate groups of dendronized IONPs

A carbodiimidation reaction was carried out to conjugate the TL (P22 molecule: Figure 3A) at the DNP surface. The typical reaction proceeds in two steps as shown in Figure 3B.

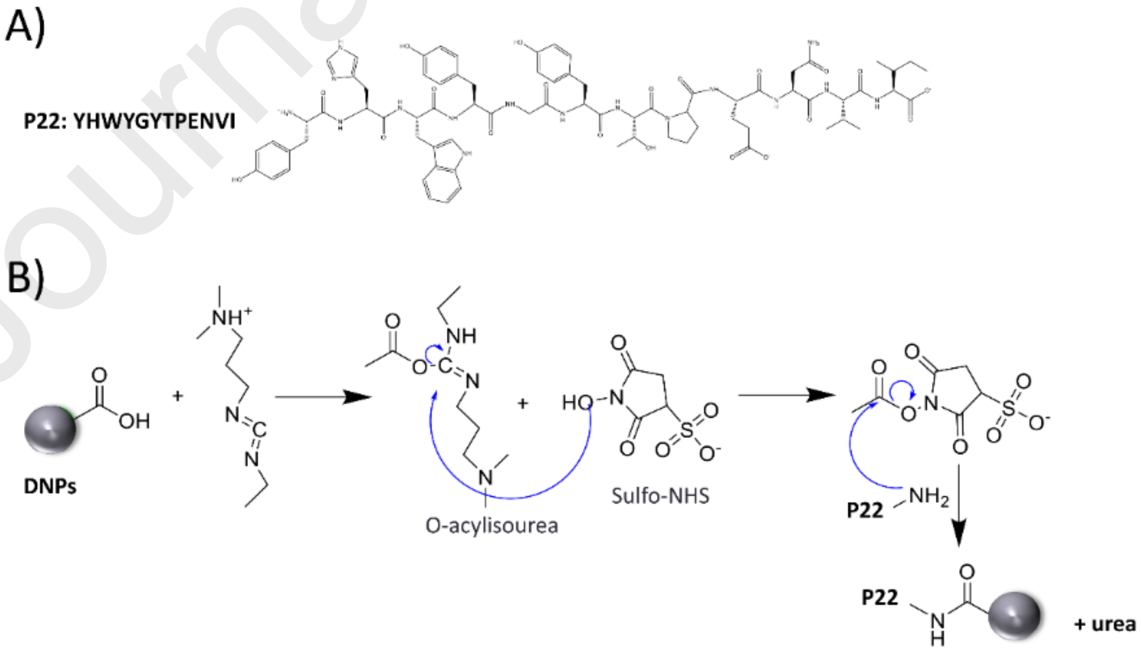

Figure 3 : A) Chemical structure of P22 B) Carbodiimation reaction: first step: activation of the carboxylate groups at the DNP surface. Second step: amide bond formation between the active carboxylates and primary P22 amine groups.

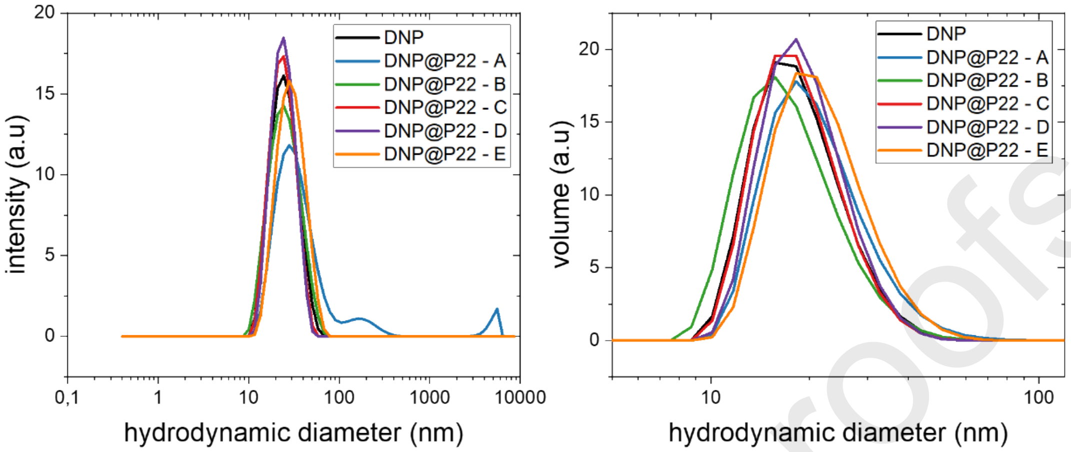

Figure 4: Mean hydrodynamic size distribution measured by DLS after the coupling reactions for the different protocols (A-E) with 0.6 molar equivalent of P22 compared to the carboxylate groups present on the dendron molecule. A) Hydrodynamic size distribution in intensity, B) Hydrodynamic size distribution in volume.

Several protocols were carried out with the aim of finding the optimal conditions to do the coupling reaction between the TL (P22) and the dendron molecules at the surface of the DNPs. Overall, five different protocols were carried out (protocols A to E) and the suspensions obtained are named respectively: DNP@P22-A, DNP@P22-B, DNP@P22-C, DNP@P22-D, DNP@P22-E. The reaction conditions for each protocol are described in Table 1 for 0.6 molar equivalents of P22. During the optimization of the coupling protocol, we noticed how relevant it is to pay attention to the stability of the EDC over time and to prevent it from hydrolyzation with air ambient water. We recommend to order smaller amounts of EDC, have them shipped desiccated, store aliquoted and use within 6 months. Once you receive EDC, avoid moisture from entering the vial, let the EDC to attain room temperature for at least 1 hour before opening the vial and before the intended usage.

Table 1. From A to E, five different conditions evaluated for the carbodiimidation reaction between the carboxylate group of the dendron and the primary amine of the P22 TL.

	DNPs + P22 A	**DNPs + P22 B**	**DNPs + P22 C**	**DNPs + P22 D**	**DNPs + P22 E**
Coupling conditions	EDC only (molar ratio	EDC only (molar ratio	EDC only (molar ratio	EDC + sulfo-NHS (molar ratio compared	EDC + sulfo-NHS (molar ratio compared

	compared to Dendron: 20:1)	compared to Dendron: 20:1)	compared to Dendron: 20:1)	to Dendron: 20:1)	to Dendron: 20:1)
	In milliQ water	In milliQ water	In milliQ water	In milliQ water	HEPES and carbonate buffer
	No pH control	No pH control	pH controlled with NaOH (brought to 9 after P22 addition)	pH controlled with NaOH (brought to 9 after P22 addition)	pH controlled with buffers
	No washing after EDC addition	Addition of a washing step after EDC activation	Addition of a washing step after EDC activation	Washing step after EDC + s-NHS activation	Washing step after EDC + s-NHS activation

At the beginning, both (activation and coupling) steps were conducted in water without a precise pH control (e.g., protocols A and B). We did not see clearly neither the appearance of characteristics peaks by FTIR spectroscopy, nor high changes in hydrodynamic size (D_h) by DLS or zeta potential value variations. Nevertheless, with the protocol A by comparison with protocol B, slight variations are observed suggesting some P22 coupling (Table 2). Indeed, as the P22 molecule is not a big molecule, it is not so easy to confirm its presence by DLS measurements (Figure 4). For the one pot protocol A, some aggregates were sometimes observed (aggregates with D_h higher than100 nm in Figure 4), that we suspect to be due to a copolymerization of P22 (binding to P22 molecules already bound to a single NP binding between P22 molecules or crosslinking peptide molecules of several NPs) as no wash was performed between the two steps. Indeed, as EDC was not removed before adding P22, it may also activate the carboxylate groups present on the peptide and therefore lead to polymerization between peptides molecules. This shouldn't be the case for protocol B that includes an EDC washing step prior P22 addition. The DLS curve in Figure 4 confirms this.

Table 2. pH conditions for each protocol, mean hydrodynamic size (D_h) and zeta potential value at pH 6.5 after the coupling step performed with 0.6 molar equivalents of P22 as a function of each protocol detailed in Table 1 and percentage of the P22 coupling as determined by HPLC-UV (ND: not determined, *: water, ^{b}: buffer).

Samples	DNPs	A	B	C	D	E
pH 1st step 2nd step		no pH control*	no pH control*	6-7* 9*	6-7* 9*	6.5^b 9.2^b
D_h (nm)	18.7	20.6	17.4	18.7	20.1	21.7
ΔD_h	-	1.9	-	0	1.4	3

Zeta potential ζ value (mV)	-22	-29	-22	-22	-35	-42
Δζ	-	-7	0	0	-13	-20
% of coupling		ND	40 %	50 %	25 %	45 %

The consideration of the reported pHs used for some EDC/NHS reactions in published papers (Table 3) evidenced strong discrepancies in the pH values. When mostly referring to the coupling of biomolecules to inorganic NPs, a diversity of pH conditions could be observed for carbodiimide reactions of the type here applied. The pH was either mainly in the range 5-6 or 8-10 for both activation and coupling reactions. Some protocols rely on the use of EDC only and some add NHS or its water soluble version, sulfo-NHS, prior coupling of biomolecules. NHS addition can be done in parallel with EDC (one pot reaction) or subsequently. Reaction time and temperature are also highly variable. In addition, the coupling is reported at room temperature or assisted by microwave. After carefully considering, the chemical details of the two steps of the reaction, discussing with organic chemists, going back to the main literature sources[62] and performing several trials, we finally established that the activation and coupling reactions had to be performed at different pH ranges: 5-6 and 8-10 respectively.

Table 3. Reported pH range for carbodiimide reactions according to the literature. pHa: pH during the activation reaction, pHc: pH during the coupling reaction, one pot: EDC and NHS (or sulfo-NHS) added simultaneously.

Reference	Solvent	Molecules	EDC	NHS	sNHS	pHa	time	Temp	pHc	time	Temp
63	Sodium tetraborate 50 mM	cRGD + Iron oxideNPs	Yes	-	-	9	2 h	RT		2h	35 C
64	water	cRGD + NPs	Yes	Yes	-	no info	4 h	RT	no info	24 h	RT
65	Dry DMSO	cRGD + NPs	Yes	Yes	-	-	24 h	RT			
62	MES 0.1 M	Proteins + amines	Yes	-	-	4.7	2 h	RT			
66	-	cRGD + IONPs	Yes	Yes	-	4	no info	no info	9	3 cycles 5’	65 C MW
67	-	cRGD + IONPs	Yes	Yes	-	4	no info	no info	9	3 cycles 3’	65 C MW
68	water	cRGD + IONPs	Yes	Yes		4	2 h	RT	9	overnight	RT
69	PBS 50mM	IONP + Alendronate	Yes	Yes		7	30 min + (2 h washing by dyalisis)	RT	7	3 h	RT
20	water	IONP + Alexa dye	Yes			No info	30min			1 h after addition of dye	
70	water	Stelate mesoporous silica + quantum dots	Yes	Yes		7	One pot (4hrs)				
71	MES 0.1 M / DMSO		Yes	Yes	-	6	3 h				
72	Sodium borate	peptide + Gold NPs	Yes	-	Yes	9	24 h	RT	One pot		
73	PBS 0.01 M	NPs + polylisine	Yes	Yes	-	no info	1 h	RT	no info	12 h	45 C
74	MES 0.1 M	NPs + Ab	Yes	Yes	-	6.2	2 h	RT	6.2	4h	no info
75	PBS 0.01 M	SPIONs + dye	Yes	-	Yes	7.2	10 min	no info	7.2	3 h	25 C
76	PBS 0.01 M	NPs + Ab	Yes	Yes	-	no info	90 min	RT	no info	2h 30'	RT

[77]	DMF	CDs + IONPs	Yes	Yes	-	-	1 h	RT		24 h	RT
[27]	water	NPs + NH2-DOTA	Yes	-	-	6.5	30 min	0 C	6.5	2 h	RT
[78]	MOPS 50 mM + NaCl 50 mM	Peptides	Yes	-	Yes	7.1	20 h	RT	One pot		
[79]	no info	NPs+DOTA+linker	Yes	-	Yes	5.5	30 min		8.5	1 h	4 C
[62]	MES 50 mM	NPs -COOH + R-NH2	Yes	-	Yes	6	2-4 h	RT	One pot		
[62]	MES 50 mM	NPs -COOH + R-NH2	Yes	-	Yes	6	15 min	RT	6/9	2-4 h	RT

Among all the protocols in which we carefully considered the pH conditions (C to E, *Table 1*), protocol E is the one leading to higher variations in D_h and zeta potential (Table 2). Protocol D results in higher variations in D_h and zeta potential than protocol C, showing that sulfo-NHS was an important reagent for our coupling conditions. Nevertheless, one can see that the variations with protocol D are close to those of protocol A. In any case, protocol E displayed the highest change in zeta potential value toward negative values, together with a meaningful change in the mean D_h. Basically, working in buffer solutions (protocol E) instead of water (protocols A, B, C and D), we were able to better control the pH conditions in both steps. An acidic pH of 6.5 for the carboxylate activation, with the addition of EDC first, alone for 10 min and in concentrated conditions (both for EDC and for the DNPs), followed by the addition of sulfo-NHS for 20 additional minutes were the optimal conditions for the first step. As expected, the absence of EDC washing out prior the addition of the peptide can be linked to a potential undesired copolymerization of the peptide, as already discussed. The overall time for the activation step was kept low (30 min), and the temperature at 24°C. After thorough washing of unreacted EDC, sulfo-NHS and reaction products, with a buffer at higher pH than for step 1, samples were quickly recovered in the least possible volume and exposed to the peptide. For this second step, we increased the pH until 9.2 where we are close to the pKa of primary amines.

To favour a high coupling yield, the peptide molar ratio to the carboxylate groups in the dendron was varied. We have tested three different P22 amounts: 0.25, 0.6 and an excess with 1.2 molar equivalents of P22 with respect to the number of activated carboxylates present on the DNPs. Most experiments have been performed with the molar ratio 0.6, though.

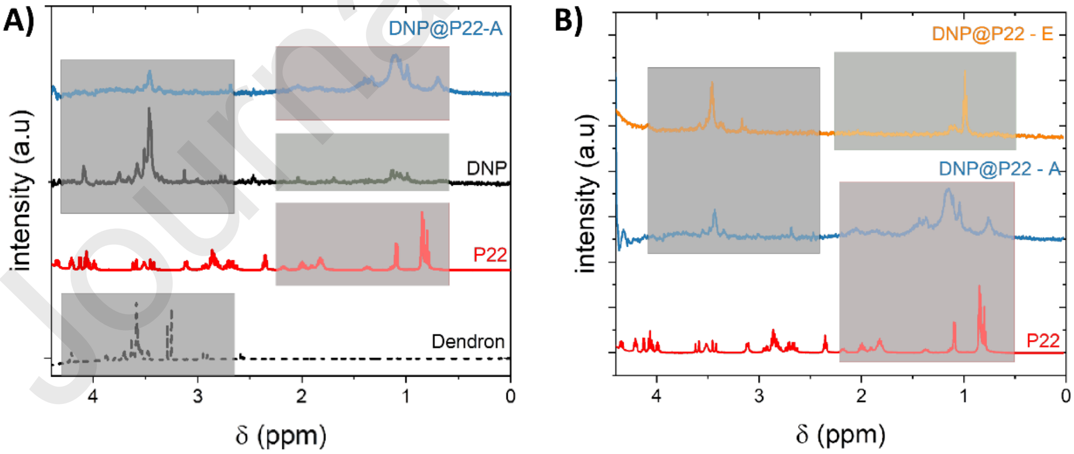

Figure 5: A) comparison of HRMAS spectra of (from top to bottom): DNP@P22-A (blue), DNP (black), P22 (red) and dendron (black dots), B) Comparison of HRMAS spectra of (from top to bottom): DNP@P22 – optimized protocol E (orange), DNP@P22 – A (blue) and P22 (red).

In the HRMAS spectra in Figure 5, the presence of the dendron on DNPs/DNPs@P22 is evidenced for both conditions (protocols A and E). The signal of P22 is clearer for protocol E compared to protocol A and that can be due to the suspected copolymerization taking place with protocol A. Nevertheless, by HRMAS, it was not possible to unambiguously confirm the presence of the peptide neither to quantify it.

The NMRD profile corresponds to the measurement of the proton relaxivity r_1 as a function of the proton Larmor frequency in an IONPs suspension. The NMRD profiles of superparamagnetic IONPs have a characteristic shape from which one can extract, after their fitting, different structural and magnetic parameters of the IONPs such as the saturation magnetization (M_s), or the NMRD radius. These two parameters depend on how close the water protons are from the magnetic core of IONPs. The coating of the IONPs can affect the distance between proton and magnetic core and thus the NMRD profile. The denser the coating is, the farther the protons will be from the core. Thereby, smaller M_s values and bigger radius will be determined from NMRD measurements. Here, the radius determined from the fitting of the NMRD profile is quite close to the radius determined after TEM images analysis (Table 4). Indeed, the dendron with its three PEG branches allows a lot of mobility and the water molecules can easily move toward the core of the NPs[20].

Adding the P22 at the surface of DNPs could hinder this mobility and thus decrease both the Ms and the radius determined by NMRD. As seen in Table 4 and Figure 6, this effect is more visible for protocol A, where we suspect that a copolymerization happens between the P22 molecules. Indeed, the measured M_s is only 37.5 emu/g compared to 46.8 emu/g before coupling. As for the radius, it goes from 6.9 nm for DNPs to 7.9 nm when the peptide is coupled with protocol A. This strong difference tends to validate the copolymerization theory, which is happening with the protocol A. The effect is less marked for the protocol E, where the radius determined by the NMRD profile fitting shows only an increase of 0.4 nm after the P22 coupling and the M_s is also less impacted by the presence of P22 (47.8 emu/g compared to 49.9 emu/g before coupling). These results seem to agree with the fact that with protocol A, copolymerized P22 are on the DNPs surface whereas for protocol E, P22 is coupled without this copolymerization phenomenon.

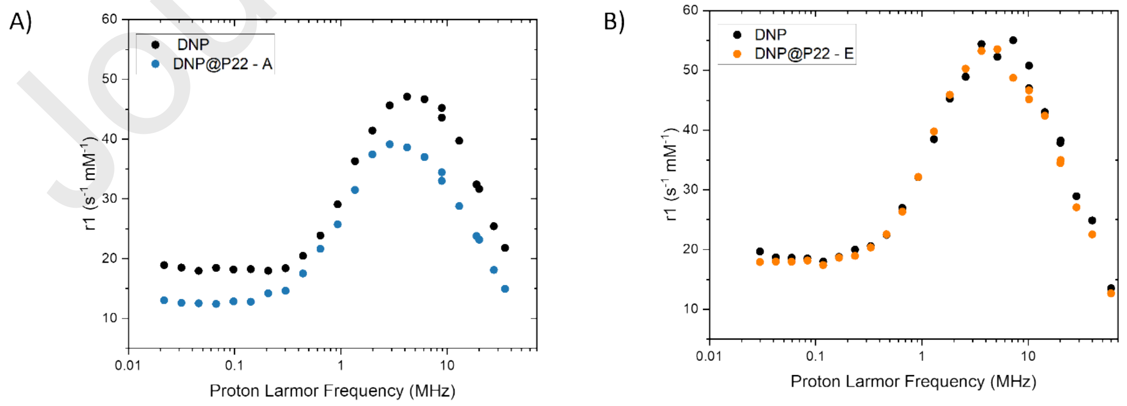

Figure 6: A) NMRD profiles of DNP (black) and DNP@P22-A (blue), B) NMRD profiles of DNP (black) and DNP@P22 -E (orange).

Table 4: TEM radius, NMRD radius and M_s determined after NMRD profile fitting for four suspensions: two of DNP, DNP@P22 - A and DNP@P22 -E

	DNP before protocol A	DNP@P22 - A	DNP before protocol E	DNP@P22 - E
Radius (TEM) (nm)	6.2	/	6.4	/
Radius (NMRD) (nm)	6.9	7.9	6.8	7.1
M_s (NMRD) (emu/g)	46.8	37.5	49.9	47.8

3.4 P22 quantification by HPLC-UV

Concerning peptide quantification methods, we faced many difficulties. A direct quantification can be done in specific situations: for example, if the attached molecule is fluorescent, it can be measured by fluorescence microscopy. Otherwise, it could be measured relying on methods that quantify the protein content in solution (e.g. BCA test) or by an ELISA-type of test with an antibody that recognizes the peptide[29,70,80]. Another technique could be elemental analysis, but in our case, it is not useful because we have the same elements (C, N, O) in the dendron and in the P22. Lastly, as IONPs are magnetic, NMR is not an appropriate technique.

As an alternative, we decided to develop an indirect quantification method. Briefly, knowing the initial amount of P22 in the coupling reaction, the unbound P22 was quantified by HPLC-UV. To determine the amount of unbound P22, the supernatant (S) and the three consequent washes (W1, W2, and W3, all in water) were analyzed by HPLC-UV. The separation of the DNPs@P22 from the free P22 was done using Amicon filter tubes with a cut-off of 30 kDa and centrifugation at 8000 rpm for 5 min (Figure S4). A calibration curve for P22 was obtained in milliQ water (Figure S5). Quantification was carried out by peak integration of the chromatogram peak corresponding to P22 at an elution time of 10.2 min.

The supernatant and the washes are weighted, so, knowing the mass and the concentration by HPLC-UV, the µg of unbound P22 were obtained. The difference between the initial mass and the mass found by HPLC measurements allowed to calculate the number of molecules of P22 bound to the dendron at the DNPs surface. This quantification was possible for protocols B to E but not for A. Indeed, with protocol A, the HPLC chromatogram does not display a single peak as with all other protocols, but several peaks possibly due to the polymerization of P22 (Figure S6).

The P22 coupling yield was estimated for protocols B to E. For all protocols, the coupling is around 40% except for protocol D where only 25% coupling is noticed. This lower coupling amount could be explained by the more difficult pH control by adding HCl and NaOH to water, which may have perturbed the reaction. However, it is important to underline that these coupling yields may have been overestimated as some peptide could be retained in the filters of the Amicon tubes. The amount of P22 bound to the filter is hard to quantify accurately. Otherwise, this quantification method allows for a fair comparison between the different samples as they were treated equally. The comparison of the D_h and zeta potential values and of the percentage of P22 coupling (Table 3) shows that, for protocol B, a coupling of 40% is obtained when no variation in D_h and zeta potential value is observed. By contrast, with the protocol D, a variation in these values is observed (quite similar to that of protocol A) but the coupling percentage is rather low. This may perhaps be attributed to an interaction of P22 with PEG chains like a “burial” of P22 in PEG chains depending on the protocol. The highest variations in mean hydrodynamic size and zeta potential values were observed with the protocol E. Furthermore, protocol E had the best reproducibility: it was assessed several times with various molar equivalents of P22 compared to carboxylate groups: 0.25, 0.6 and 1.2 molar equivalents, as it can be observed in Figure 7. With this protocol, the amount of coupled P22 increased for increasing P22 molar equivalents (19.5, 45 and 37.5% for 0.25, 0.6 and 1.2 molar equivalents, respectively), though one may notice that the coupling with an excess of P22 does not imply more coverage. Indeed, it seems that the coupling maximum is around 40 %, which may be explained by some steric hindrance at the surface of DNPs.

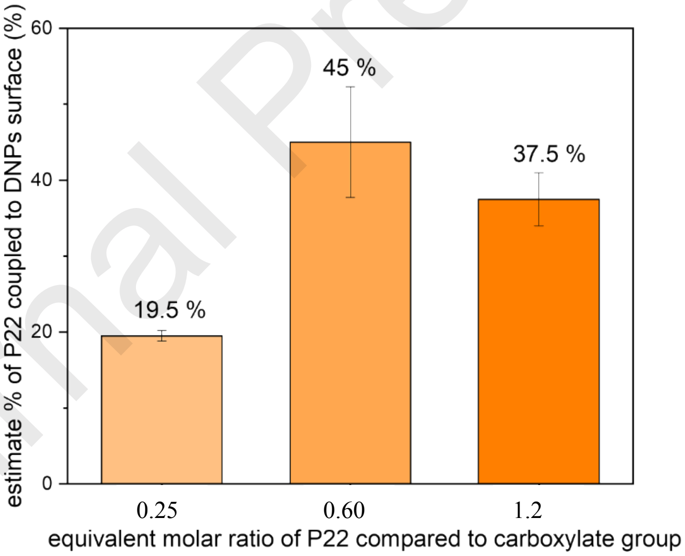

Figure 7: Estimation of P22 coupling after protocol E with 0.25, 0.6 and 1.2 equivalent of P22. The bars show the mean percentage with their respective standard deviations.

3.5 Cell internalization studies

Before investigating the cell internalization of DNPs and DNPs@P22 in *in vitro* studies, we first carried out cytotoxicity tests on a panel of DNPs@P22 made according to different protocols. After that, DNPs and DNPs@P22 were exposed to the cells to evaluate their cell uptake.

3.5.1 Cytotoxicity study

Cytotoxicity of both suspensions (DNPs and DNPs@P22) was evaluated by the MTT assay using two head and neck cancer cell lines: 93-Vu and FaDu. Cells were incubated for 24 h with the suspensions at various concentrations (from 0 to 400 µg/mL of iron). DNPs@P22 were prepared according to protocol E with a 0.6 P22 molar equivalent. As observed in Figure 8, DNPs do not show remarkable cytotoxicity up to 200 µg Fe/mL. Up to a concentration of 100µgFe/mL, the presence of the peptide reduces cell viability compared to the dendronized NPs, but this decrease in cell viability remains well tolerated by cells: cells decrease their mitochondrial activity but there are no appreciable changes in cell amount on the wells neither cells detached. The situation changes with concentrations higher than 100µgFe/mL for which cell viability decreases to values below 70%.

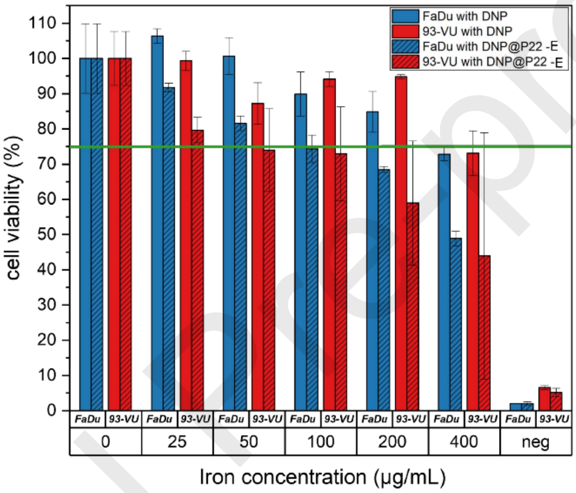

Figure 8: Cell viability of FaDu (blue) and 93-VU (red) cell monolayers as a function of the amount of DNPs and DNPS@P22–E. Neg: negative control with DMSO.

3.5.2 Internalization study

Cell internalization studies have been conducted at a Fe concentration of 100 µg/mL, which is below the concentrations inducing noticeable cytotoxicity. As a time point, 24 h was the time chosen to study the internalization of DNPs or DNPs@P22 in both cell lines (FaDu and 93-VU).

With protocols A and E, when the amount of P22 increases up to 0.6 equivalent of P22 (coverage around 45% for protocol E), internalization was observed but its amount seems to depend on the concentration and also, on the protocol. Indeed, with protocol A, a higher internalization is observed in comparison with DNPs without P22. The comparison between protocols A and E shows that protocol A leads to higher internalization values with 0.6 equivalent of P22 at a concentration of 100 µgFe/mL (Figure 9). Higher internalization amounts are observed with the optimized protocol E and a P22 equivalent of 1.2 (instead of 0.6) and a concentration of 100 µgFe/mL (Figure 10).

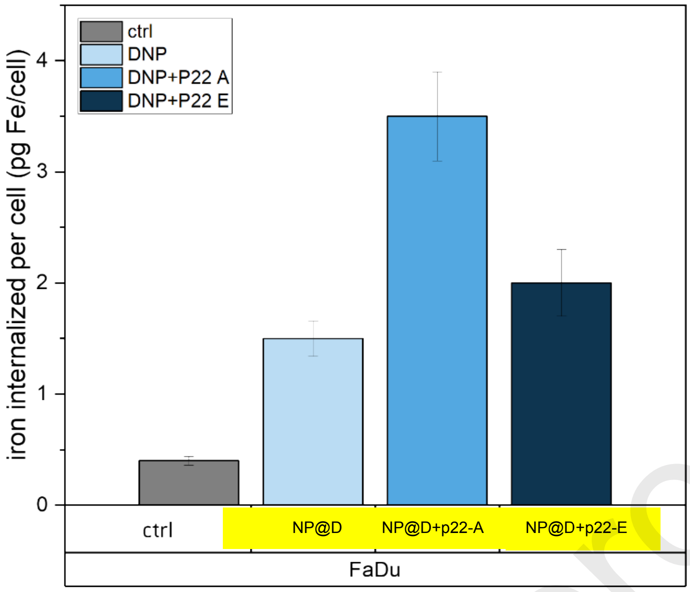

Figure 9: Amount of iron internalized by FaDu cells with DNPs and DNPs@P22 prepared with the protocol A (DNP@P22 – A) and protocol E (DNP@P22 – E) with 0.6 molar equivalent of P22 compared to the carboxylate groups present on DNPs' surface. IONP concentration: 100 µg Fe/mL.

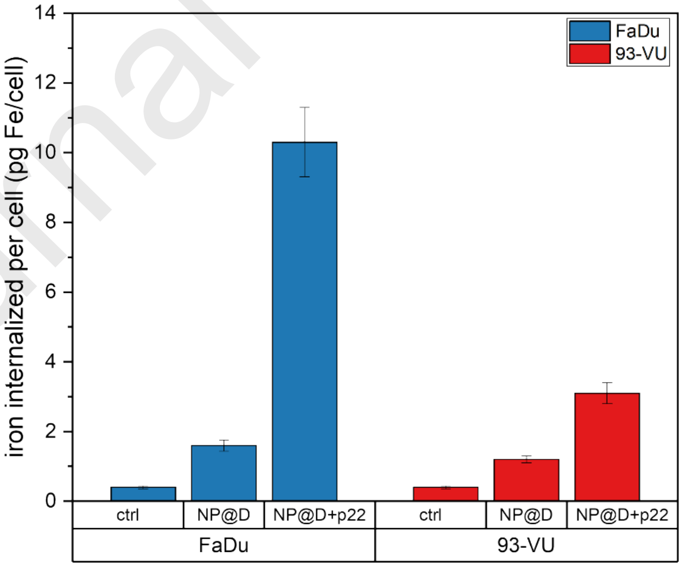

Figure 10: Amount of iron internalized by FaDu and 95-Vu cells with DNPs and DNPs@P22 prepared with the protocol E and a P22 molar equivalent of 1.2 (coverage 37.5%). NP concentration: 100 µgFe/mL).

The effect of the presence of P22 is clearly visible for both cell lines and especially for the FaDu line as the amount of pg Fe/cell is higher. Indeed, about 10 pg of iron per cell are found with DNPs bearing the P22 against 1.6 pg for DNPs without P22. The 93-VU cell line seems less prone to the effect of targeting provided by the peptide. The amount of EGF receptors in both cell lines will be compared in the future to try to explain such differences.

Among all protocols, the protocol A, where a copolymerization of P22 is suspected, and the protocol E, with a P22 equivalent of 1.2 instead of 0.6, which leads however to almost the same P22 coverage, have conducted to cell internalization. Our hypothesis is that these coupling conditions may favor an interaction between P22 molecules and the EGFR in cells. P22 molecules are coupled on DNPs but there are possibly other P22 molecules interacting strongly with them and probably more available for interacting with cells as depicted on Figure 11 The 1.2 molar excess of P22 with respect to the carboxylate functions present on the NP surface enables peptide-peptide interactions that are probably not present at 0.6 molar equivalent. This interactions may end up creating either a push-out of the peptide from the NP surface or a higher local density of P22 molecules that favors TL recognition by the cells. This peptide is quite short (twelve amino acids: linear up ~ 7 nm but certainly folded ~ 2-3 nm in length) with similar length than the dendron if it is folded and presents several hydrophobic residues that may tend to fold it in aqueous medium and therefore to shorten it. This particular conformation of the peptide on the surface of the NP may prompt its better recognition by cells, and therefore the higher NP uptake observed for 1.2 as compared to 0.6 as molar equivalents. Adding a spacer to the peptide could promote its distancing from the NP surface and hence its effective recognition by the target cells.

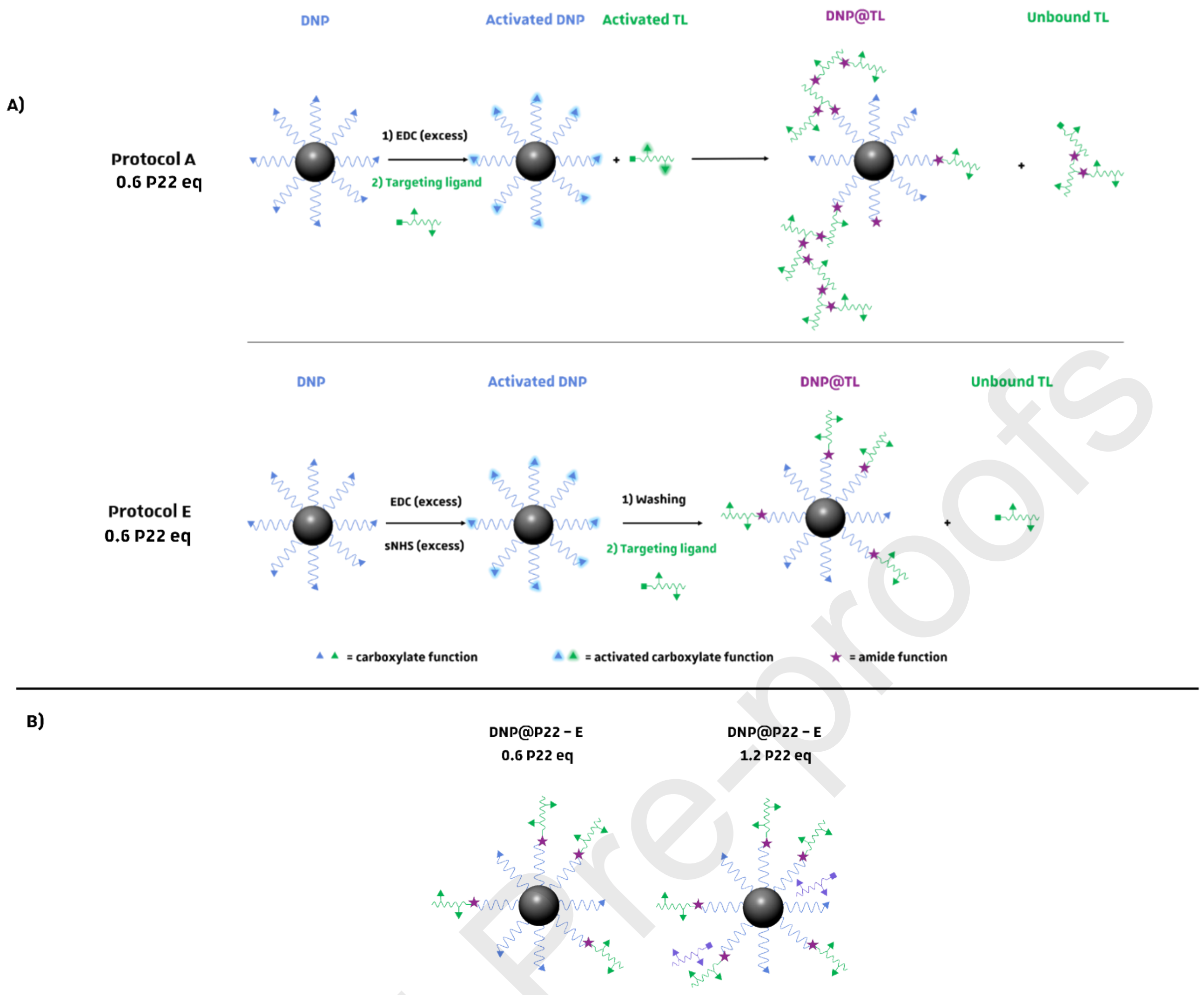

Figure 11 Hypothesis about P22 coverage to explain in vitro internalization results for A) protocols A and E with 0.6 P22 molar equivalent compared to dendron molecules and B) protocol E with either 0.6 or 1.2 P22 molar equivalent compared to dendron molecules. In protocol A, the EDC is not washed after NP activation. Therefore, it remains in solution to potentially activate carboxylate groups in the TL. In protocol E, EDC and s-NHS are removed after NP activation.

Overall, the *in vitro* studies confirmed the need of P22 targeting ligand to increase DNPs internalization inside cancerous cells that overexpress the EGF receptor. This is in agreement with other previous studies based on iron-oxide nanoparticles coupled with GE11 (original peptide from which P22 was derived) that suggested the strong role of the peptide to increase nanoparticle accumulation inside cells.[81,82] Otherwise, the internalized amount of DNPs needs to be increased for ensuring an efficient diagnosis and therapy and the introduction of a spacer between DNPs surface and the P22 TL should allow enhancing the peptide-cell recognition and thus DNPs internalization.

5. Conclusions

In this work, we highlighted the difficulties in coupling and quantifying a peptide grafted on the surface of DNPs. Even if carbodiimide reactions are widely used, their experimental conditions are not trivial as evidenced by the discrepancies observed for the pH conditions of coupling, the used temperatures (4°C, room temperature or assisted by microwave), the washings between the activation and coupling steps, and the use of reactents (*e.g.,* with or without sulfo-NHS). The stability and/or ageing of EDC was found to be a crucial point to have efficient and reproducible couplings as well as the careful control of the pH during the activation and coupling steps. This optimization allowed us to establish a reproducible protocol leading to a controlled amount of peptide grafted at the surface of DNPs. The amount of P22 has been determined by an indirect method and may slightly be overestimated due to the observed loss of P22 during the different washing steps, mostly in the centrifugation membranes. Nevertheless, the obtained amount of coupled P22 is reproducible. The first *in vitro* studies have confirmed that there is an enhancement in the uptake of DNPs@P22, compared to DNPs without TL. These *in vitro* studies with two head and neck cancer cell lines also underlined the importance of peptide amount and peptide conformation on the NP surface to propel cell recognition and further uptake. Such observations suggested that the TLs need to be highly accessible for cancer cells receptors and not too close from the surface of DNPs to facilitate nanoparticles internalization. Further experiments will be conducted by introducing a PEG spacer between DNPs and the peptide to enhance the DNPs cell internalization.

Acknowledgements

The Region Alsace, France, and the University of Mons are gratefully acknowledged for the doctoral fellowship to Barbara Freis. This project received funding from ANR (EURONANOMED2020-121 - THERAGET) under the umbrella of the ERA-NET EuroNanoMed (GA N°723770) of the EU Horizon 2020 Research and Innovation and ProtherWal "Walloon Region via the ProtherWal Society (Agreement 7289). SuperBranche is thanked for providing dendron molecules. M.T. acknowledges support from CONICET (Argentina) and from the Ministry of Science, Technology and Innovation. UMONS acknowledges the financial support of the Fond National de la Recherche Scientifique (FNRS), the ARC Programs of the French Community of Belgium, COST actions and the Walloon region (ProtherWal and Interreg projects). S.F. acknowledges UMONS, EpiCURA Hospital, ProtherWal and the Fund for Medical Research in Hainaut (FRMH). The authors thank the XRD platform of the IPCMS.

REFERENCES

(1) Attia, M. F.; Anton, N.; Wallyn, J.; Omran, Z.; Vandamme, T. F. An Overview of Active and Passive Targeting Strategies to Improve the Nanocarriers Efficiency to Tumour Sites. *Journal of Pharmacy and Pharmacology* **2019**, *71* (8), 1185–1198. https://doi.org/10.1111/jphp.13098.

(2) Bazak, R.; Houri, M.; El Achy, S.; Kamel, S.; Refaat, T. Cancer Active Targeting by Nanoparticles: A Comprehensive Review of Literature. *J Cancer Res Clin Oncol* **2015**, *141* (5), 769–784. https://doi.org/10.1007/s00432-014-1767-3.

(3) Yu, M. K.; Park, J.; Jon, S. Targeting Strategies for Multifunctional Nanoparticles in Cancer Imaging and Therapy. *Theranostics* **2012**, *2* (1), 3–44. https://doi.org/10.7150/thno.3463.

(4) Matsumura, Y.; Maeda, H. A New Concept for Macromolecular Therapeutics in Cancer Chemotherapy: Mechanism of Tumoritropic Accumulation of Proteins and the Antitumor Agent Smancs. *Cancer Res* **1986**, *46* (12 Pt 1), 6387–6392.

(5) Ahmad, A.; Khan, F.; Mishra, R. K.; Khan, R. Precision Cancer Nanotherapy: Evolving Role of Multifunctional Nanoparticles for Cancer Active Targeting. *J. Med. Chem.* **2019**, *62* (23), 10475–10496. https://doi.org/10.1021/acs.jmedchem.9b00511.

(6) Makhani, E. Y.; Zhang, A.; Haun, J. B. Quantifying and Controlling Bond Multivalency for Advanced Nanoparticle Targeting to Cells. *Nano Convergence* **2021**, *8* (1), 38. https://doi.org/10.1186/s40580-021-00288-1.

(7) Byrne, J. D.; Betancourt, T.; Brannon-Peppas, L. Active Targeting Schemes for Nanoparticle Systems in Cancer Therapeutics. *Advanced Drug Delivery Reviews* **2008**, *60* (15), 1615–1626. https://doi.org/10.1016/j.addr.2008.08.005.

(8) Allen, T. M. Ligand-Targeted Therapeutics in Anticancer Therapy. *Nat Rev Cancer* **2002**, *2* (10), 750–763. https://doi.org/10.1038/nrc903.

(9) Angelopoulou, A.; Kolokithas-Ntoukas, A.; Fytas, C.; Avgoustakis, K. Folic Acid-Functionalized, Condensed Magnetic Nanoparticles for Targeted Delivery of Doxorubicin to Tumor Cancer Cells Overexpressing the Folate Receptor. *ACS Omega* **2019**, *4* (26), 22214–22227. https://doi.org/10.1021/acsomega.9b03594.

(10) Truffi, M.; Colombo, M.; Sorrentino, L.; Pandolfi, L.; Mazzucchelli, S.; Pappalardo, F.; Pacini, C.; Allevi, R.; Bonizzi, A.; Corsi, F.; Prosperi, D. Multivalent Exposure of Trastuzumab on Iron Oxide Nanoparticles Improves Antitumor Potential and Reduces Resistance in HER2-Positive Breast Cancer Cells. *Sci Rep* **2018**, *8* (1), 6563. https://doi.org/10.1038/s41598-018-24968-x.

(11) Yoo, J.; Park, C.; Yi, G.; Lee, D.; Koo, H. Active Targeting Strategies Using Biological Ligands for Nanoparticle Drug Delivery Systems. *Cancers* **2019**, *11* (5), 640. https://doi.org/10.3390/cancers11050640.

(12) Tietjen, G. T.; Bracaglia, L. G.; Saltzman, W. M.; Pober, J. S. Focus on Fundamentals: Achieving Effective Nanoparticle Targeting. *Trends in Molecular Medicine* **2018**, *24* (7), 598–606. https://doi.org/10.1016/j.molmed.2018.05.003.

(13) NDong, C.; Tate, J. A.; Kett, W. C.; Batra, J.; Demidenko, E.; Lewis, L. D.; Hoopes, P. J.; Gerngross, T. U.; Griswold, K. E. Tumor Cell Targeting by Iron Oxide Nanoparticles Is Dominated by Different Factors In Vitro versus In Vivo. *PLoS ONE* **2015**, *10* (2), e0115636. https://doi.org/10.1371/journal.pone.0115636.

(14) Palanisamy, S.; Wang, Y.-M. Superparamagnetic Iron Oxide Nanoparticulate System: Synthesis, Targeting, Drug Delivery and Therapy in Cancer. *Dalton Trans.* **2019**, *48* (26), 9490–9515. https://doi.org/10.1039/C9DT00459A.

(15) Mittelheisser, V.; Coliat, P.; Moeglin, E.; Goepp, L.; Goetz, J. G.; Charbonnière, L. J.; Pivot, X.; Detappe, A. Optimal Physicochemical Properties of Antibody–Nanoparticle Conjugates for Improved Tumor Targeting. *Advanced Materials* **2022**, *34* (24), 2110305. https://doi.org/10.1002/adma.202110305.

(16) Alphandéry, E. Biodistribution and Targeting Properties of Iron Oxide Nanoparticles for Treatments of Cancer and Iron Anemia Disease. *Nanotoxicology* **2019**, *13* (5), 573–596. https://doi.org/10.1080/17435390.2019.1572809.

(17) Wilhelm, S.; Tavares, A. J.; Dai, Q.; Ohta, S.; Audet, J.; Dvorak, H. F.; Chan, W. C. W. Analysis of Nanoparticle Delivery to Tumours. *Nat Rev Mater* **2016**, *1* (5), 1–12. https://doi.org/10.1038/natrevmats.2016.14.

(18) Basly, B.; Felder-Flesch, D.; Perriat, P.; Billotey, C.; Taleb, J.; Pourroy, G.; Begin-Colin, S. Dendronized Iron Oxide Nanoparticles as Contrast Agents for MRI. *Chemical Communications* **2010**, *46* (6), 985–987. https://doi.org/10.1039/B920348F.

(19) Ghobril, C.; Popa, G.; Parat, A.; Billotey, C.; Taleb, J.; Bonazza, P.; Begin-Colin, S.; Felder-Flesch, D. A Bisphosphonate Tweezers and Clickable PEGylated PAMAM Dendrons for the Preparation of Functional Iron Oxide Nanoparticles Displaying Renal and Hepatobiliary Elimination. *Chemical Communications (Cambridge, England)* **2013**, *49* (80), 9158–9160. https://doi.org/10.1039/c3cc43161d.

(20) Walter, A.; Garofalo, A.; Parat, A.; Jouhannaud, J.; Pourroy, G.; Voirin, E.; Laurent, S.; Bonazza, P.; Taleb, J.; Billotey, C.; Elst, L. V.; Muller, R. N.; Begin-Colin, S.; Felder-Flesch, D. Validation of a Dendron Concept to Tune Colloidal Stability, MRI Relaxivity and Bioelimination of Functional Nanoparticles. *J. Mater. Chem. B* **2015**, *3* (8), 1484–1494. https://doi.org/10.1039/C4TB01954G.

(21) Walter, A.; Billotey, C.; Garofalo, A.; Ulhaq-Bouillet, C.; Lefèvre, C.; Taleb, J.; Laurent, S.; Vander Elst, L.; Muller, R. N.; Lartigue, L.; Gazeau, F.; Felder-Flesch, D.; Begin-Colin, S. Mastering the Shape and Composition of Dendronized Iron Oxide Nanoparticles To Tailor Magnetic Resonance Imaging and Hyperthermia. *Chemistry of Materials* **2014**, *26* (18), 5252–5264. https://doi.org/10.1021/cm5019025.

(22) Walter, A.; Garofalo, A.; Bonazza, P.; Meyer, F.; Martinez, H.; Fleutot, S.; Billotey, C.; Taleb, J.; Felder-Flesch, D.; Begin-Colin, S. Effect of the Functionalization Process on the Colloidal, Magnetic Resonance Imaging, and Bioelimination Properties of Mono- or Bisphosphonate-Anchored Dendronized Iron Oxide Nanoparticles. *ChemPlusChem* **2017**, *82* (4), 647–659. https://doi.org/10.1002/cplu.201700049.

(23) Cotin, G.; Blanco-Andujar, C.; Nguyen, D.-V.; Affolter, C.; Boutry, S.; Boos, A.; Ronot, P.; Uring-Lambert, B.; Choquet, P.; Zorn, P. E.; Mertz, D.; Laurent, S.; Muller, R. N.; Meyer, F.; Felder Flesch, D.; Begin-Colin, S. Dendron Based Antifouling, MRI and Magnetic Hyperthermia Properties of Different Shaped Iron Oxide Nanoparticles. *Nanotechnology* **2019**, *30* (37), 374002. https://doi.org/10.1088/1361-6528/ab2998.

(24) Cotin, G.; Blanco-Andujar, C.; Perton, F.; Asín, L.; de la Fuente, J. M.; Reichardt, W.; Schaffner, D.; Ngyen, D.-V.; Mertz, D.; Kiefer, C.; Meyer, F.; Spassov, S.; Ersen, O.; Chatzidakis, M.; Botton, G. A.; Hénoumont, C.; Laurent, S.; Greneche, J.-M.; Teran, F. J.; Ortega, D.; Felder-Flesch, D.; Begin-Colin, S. Unveiling the Role of Surface, Size, Shape and Defects of Iron Oxide Nanoparticles for Theranostic Applications. *Nanoscale* **2021**, *13* (34), 14552–14571. https://doi.org/10.1039/D1NR03335B.

(25) Lamanna, G.; Kueny-Stotz, M.; Mamlouk-Chaouachi, H.; Ghobril, C.; Basly, B.; Bertin, A.; Miladi, I.; Billotey, C.; Pourroy, G.; Begin-Colin, S.; Felder-Flesch, D. Dendronized Iron Oxide Nanoparticles for Multimodal Imaging. *Biomaterials* **2011**, *32* (33), 8562–8573. https://doi.org/10.1016/j.biomaterials.2011.07.026.

(26) Basly, B.; Popa, G.; Fleutot, S.; Pichon, B. P.; Garofalo, A.; Ghobril, C.; Billotey, C.; Berniard, A.; Bonazza, P.; Martinez, H.; Felder-Flesch, D.; Begin-Colin, S. Effect of the Nanoparticle Synthesis Method on Dendronized Iron Oxides as MRI Contrast Agents. *Dalton Transactions* **2013**, *42* (6), 2146–2157. https://doi.org/10.1039/C2DT31788E.

(27) Bordeianu, C.; Parat, A.; Piant, S.; Walter, A.; Zbaraszczuk-Affolter, C.; Meyer, F.; Begin-Colin, S.; Boutry, S.; Muller, R. N.; Jouberton, E.; Chezal, J.-M.; Labeille, B.; Cinotti, E.; Perrot, J.-L.; Miot-Noirault, E.; Laurent, S.; Felder-Flesch, D. Evaluation of the Active Targeting of Melanin Granules after Intravenous Injection of Dendronized Nanoparticles. *Mol. Pharmaceutics* **2018**, *15* (2), 536–547. https://doi.org/10.1021/acs.molpharmaceut.7b00904.

(28) Filippi, M.; Nguyen, D.-V.; Garello, F.; Perton, F.; Bégin-Colin, S.; Felder-Flesch, D.; Power, L.; Scherberich, A. Metronidazole-Functionalized Iron Oxide Nanoparticles for Molecular Detection of Hypoxic Tissues. *Nanoscale* **2019**, *11* (46), 22559–22574. https://doi.org/10.1039/C9NR08436C.

(29) Tasso, M.; Singh, M. K.; Giovanelli, E.; Fragola, A.; Loriette, V.; Regairaz, M.; Dautry, F.; Treussart, F.; Lenkei, Z.; Lequeux, N.; Pons, T. Oriented Bioconjugation of Unmodified Antibodies to Quantum Dots Capped with Copolymeric Ligands as Versatile Cellular Imaging Tools. *ACS Appl. Mater. Interfaces* **2015**, *7* (48), 26904–26913. https://doi.org/10.1021/acsami.5b09777.

(30) Tasso, M.; Giovanelli, E.; Zala, D.; Bouccara, S.; Fragola, A.; Hanafi, M.; Lenkei, Z.; Pons, T.; Lequeux, N. Sulfobetaine–Vinylimidazole Block Copolymers: A Robust Quantum Dot Surface Chemistry Expanding Bioimaging's Horizons. *ACS Nano* **2015**, *9* (11), 11479–11489. https://doi.org/10.1021/acsnano.5b05705.

(31) Güster, J. D.; Weissleder, S. V.; Busch, C.-J.; Kriegs, M.; Petersen, C.; Knecht, R.; Dikomey, E.; Rieckmann, T. The Inhibition of PARP but Not EGFR Results in the Radiosensitization of HPV/P16-Positive HNSCC Cell Lines. *Radiotherapy and Oncology* **2014**, *113* (3), 345–351. https://doi.org/10.1016/j.radonc.2014.10.011.

(32) Ratushny, V.; Astsaturov, I.; Burtness, B. A.; Golemis, E. A.; Silverman, J. S. Targeting EGFR Resistance Networks in Head and Neck Cancer. *Cellular Signalling* **2009**, *21* (8), 1255–1268. https://doi.org/10.1016/j.cellsig.2009.02.021.

(33) Kiseleva, A.; Beck, T. N.; Serebriiskii, I. G.; Liu, H.; Burtness, B.; Golemis, E. A. Targeting the ErbB Family in Head and Neck Cancer. In *Molecular Determinants of Head and Neck Cancer*; Burtness, B., Golemis, E. A., Eds.; Current Cancer Research; Springer International Publishing: Cham, 2018; pp 7–61. https://doi.org/10.1007/978-3-319-78762-6_2.

(34) Astsaturov, I.; Cohen, R. B.; Harari, P. M. EGFR-Targeting Monoclonal Antibodies in Head and Neck Cancer. *Current Cancer Drug Targets 6* (8), 691–710.

(35) Specenier, P.; Vermorken, J. B. Cetuximab: Its Unique Place in Head and Neck Cancer Treatment. *Biologics* **2013**, *7*, 77–90. https://doi.org/10.2147/BTT.S43628.

(36) Alsahafi, E.; Begg, K.; Amelio, I.; Raulf, N.; Lucarelli, P.; Sauter, T.; Tavassoli, M. Clinical Update on Head and Neck Cancer: Molecular Biology and Ongoing Challenges. *Cell Death Dis* **2019**, *10* (8), 540. https://doi.org/10.1038/s41419-019-1769-9.

(37) Teesalu, T.; Sugahara, K.; Ruoslahti, E. Tumor-Penetrating Peptides. *Frontiers in Oncology* **2013**, *3*.

(38) Ruoslahti, E. Tumor Penetrating Peptides for Improved Drug Delivery. *Advanced Drug Delivery Reviews* **2017**, *110–111*, 3–12. https://doi.org/10.1016/j.addr.2016.03.008.

(39) Genta, I.; Chiesa, E.; Colzani, B.; Modena, T.; Conti, B.; Dorati, R. GE11 Peptide as an Active Targeting Agent in Antitumor Therapy: A Minireview. *Pharmaceutics* **2018**, *10* (1), 2. https://doi.org/10.3390/pharmaceutics10010002.

(40) Hossein-Nejad-Ariani, H.; Althagafi, E.; Kaur, K. Small Peptide Ligands for Targeting EGFR in Triple Negative Breast Cancer Cells. *Sci Rep* **2019**, *9* (1), 2723. https://doi.org/10.1038/s41598-019-38574-y.

(41) Lozano-Pedraza, C.; Plaza-Mayoral, E.; Espinosa, A.; Sot, B.; Serrano, A.; Salas, G.; Blanco-Andujar, C.; Cotin, G.; Felder-Flesch, D.; Begin-Colin, S.; Teran, F. J. Assessing the Parameters Modulating Optical Losses of Iron Oxide Nanoparticles under near Infrared Irradiation. *Nanoscale Adv.* **2021**, *3* (22), 6490–6502. https://doi.org/10.1039/D1NA00601K.

(42) Espinosa, A.; Kolosnjaj-Tabi, J.; Abou-Hassan, A.; Plan Sangnier, A.; Curcio, A.; Silva, A. K. A.; Di Corato, R.; Neveu, S.; Pellegrino, T.; Liz-Marzán, L. M.; Wilhelm, C. Magnetic (Hyper)Thermia or Photothermia? Progressive Comparison of Iron Oxide and Gold Nanoparticles Heating in Water, in Cells, and In Vivo. *Adv. Funct. Mater.* **2018**, *28* (37), 1803660. https://doi.org/10.1002/adfm.201803660.

(43) Hermanson, G. T. *Bioconjugate Techniques*, 2nd edition.; Academic Press: San Diego, 2008.

(44) Iwasawa, T.; Wash, P.; Gibson, C.; Rebek, J. Reaction of an Introverted Carboxylic Acid with Carbodiimide. *Tetrahedron* **2007**, *63* (28), 6506–6511. https://doi.org/10.1016/j.tet.2007.03.075.

(45) Nair, D. P.; Podgórski, M.; Chatani, S.; Gong, T.; Xi, W.; Fenoli, C. R.; Bowman, C. N. The Thiol-Michael Addition Click Reaction: A Powerful and Widely Used Tool in

Materials Chemistry. *Chem. Mater.* **2014**, *26* (1), 724–744. https://doi.org/10.1021/cm402180t.

(46) Belbekhouche, S.; Guerrouache, M.; Carbonnier, B. Thiol-Maleimide Michael Addition Click Reaction: A New Route to Surface Modification of Porous Polymeric Monolith. *Macromol. Chem. Phys.* **2016**, *217* (8), 997–1006. https://doi.org/10.1002/macp.201500427.

(47) Hoyle, C. E.; Lowe, A. B.; Bowman, C. N. Thiol-Click Chemistry: A Multifaceted Toolbox for Small Molecule and Polymer Synthesis. *Chem. Soc. Rev.* **2010**, *39* (4), 1355. https://doi.org/10.1039/b901979k.

(48) Guldris, N.; Gallo, J.; García-Hevia, L.; Rivas, J.; Bañobre-López, M.; Salonen, L. M. Orthogonal Clickable Iron Oxide Nanoparticle Platform for Targeting, Imaging, and On-Demand Release. *Chem. Eur. J.* **2018**, *24* (34), 8624–8631. https://doi.org/10.1002/chem.201800389.

(49) Kolb, H. C.; Finn, M. G.; Sharpless, K. B. Click Chemistry: Diverse Chemical Function from a Few Good Reactions. *Angewandte Chemie International Edition* **2001**, *40* (11), 2004–2021. https://doi.org/10.1002/1521-3773(20010601)40:11<2004::AID-ANIE2004>3.0.CO;2-5.

(50) Pellico, J.; Gawne, P. J.; Rosales, R. T. M. de. Radiolabelling of Nanomaterials for Medical Imaging and Therapy. *Chem. Soc. Rev.* **2021**, *50* (5), 3355–3423. https://doi.org/10.1039/D0CS00384K.

(51) Nam, J.; Won, N.; Bang, J.; Jin, H.; Park, J.; Jung, S.; Jung, S.; Park, Y.; Kim, S. Surface Engineering of Inorganic Nanoparticles for Imaging and Therapy. *Advanced Drug Delivery Reviews* **2013**, *65* (5), 622–648. https://doi.org/10.1016/j.addr.2012.08.015.

(52) Rimkus, G.; Bremer-Streck, S.; Grüttner, C.; Kaiser, W. A.; Hilger, I. Can We Accurately Quantify Nanoparticle Associated Proteins When Constructing High-Affinity MRI Molecular Imaging Probes? *Contrast Media Mol Imaging* **2011**, *6* (3), 119–125. https://doi.org/10.1002/cmmi.405.

(53) Perton, F.; Cotin, G.; Kiefer, C.; Strub, J.-M.; Cianferani, S.; Greneche, J.-M.; Parizel, N.; Heinrich, B.; Pichon, B.; Mertz, D.; Begin-Colin, S. Iron Stearate Structures: An Original Tool for Nanoparticles Design. *Inorg. Chem.* **2021**, *60* (16), 12445–12456. https://doi.org/10.1021/acs.inorgchem.1c01689.

(54) Baaziz, W.; Pichon, B. P.; Fleutot, S.; Liu, Y.; Lefevre, C.; Greneche, J.-M.; Toumi, M.; Mhiri, T.; Begin-Colin, S. Magnetic Iron Oxide Nanoparticles: Reproducible Tuning of the Size and Nanosized-Dependent Composition, Defects, and Spin Canting. *J. Phys. Chem. C* **2014**, *118* (7), 3795–3810. https://doi.org/10.1021/jp411481p.

(55) Cotin, G.; Kiefer, C.; Perton, F.; Boero, M.; Özdamar, B.; Bouzid, A.; Ori, G.; Massobrio, C.; Begin, D.; Pichon, B.; Mertz, D.; Begin-Colin, S. Evaluating the Critical Roles of Precursor Nature and Water Content When Tailoring Magnetic Nanoparticles for Specific Applications. *ACS Applied Nano Materials* **2018**, *1* (8), 4306–4316. https://doi.org/10.1021/acsanm.8b01123.

(56) Cotin, G.; Kiefer, C.; Perton, F.; Ihiawakrim, D.; Blanco-Andujar, C.; Moldovan, S.; Lefevre, C.; Ersen, O.; Pichon, B.; Mertz, D.; Bégin-Colin, S. Unravelling the Thermal Decomposition Parameters for The Synthesis of Anisotropic Iron Oxide Nanoparticles. *Nanomaterials* **2018**, *8* (11), 881. https://doi.org/10.3390/nano8110881.

(57) Bordeianu, C.; Parat, A.; Affolter-Zbaraszczuk, C.; Muller, R. N.; Boutry, S.; Begin-Colin, S.; Meyer, F.; Laurent, S.; Felder-Flesch, D. How a Grafting Anchor Tailors the Cellular Uptake and in Vivo Fate of Dendronized Iron Oxide Nanoparticles. *J. Mater. Chem. B* **2017**, *5* (26), 5152–5164. https://doi.org/10.1039/C7TB00781G.

(58) Le Bail, A.; Duroy, H.; Fourquet, J. L. Ab-Initio Structure Determination of LiSbWO6 by X-Ray Powder Diffraction. *Materials Research Bulletin* **1988**, *23* (3), 447–452. https://doi.org/10.1016/0025-5408(88)90019-0.

(59) Rodríguez-Carvajal, J. Recent Advances in Magnetic Structure Determination by Neutron Powder Diffraction. *Physica B: Condensed Matter* **1993**, *192* (1), 55–69. https://doi.org/10.1016/0921-4526(93)90108-I.

(60) Boutry, S.; Forge, D.; Burtea, C.; Mahieu, I.; Murariu, O.; Laurent, S.; Vander Elst, L.; Muller, R. N. How to Quantify Iron in an Aqueous or Biological Matrix: A Technical Note. *Contrast Media Mol Imaging* **2009**, *4* (6), 299–304. https://doi.org/10.1002/cmmi.291.

(61) Walter, A.; Parat, A.; Garofalo, A.; Laurent, S.; Elst, L. V.; Muller, R. N.; Wu, T.; Heuillard, E.; Robinet, E.; Meyer, F.; Felder-Flesch, D.; Begin-Colin, S. Modulation of Relaxivity, Suspension Stability, and Biodistribution of Dendronized Iron Oxide Nanoparticles as a Function of the Organic Shell Design. *Particle & Particle Systems Characterization* **2015**, *32* (5), 552–560. https://doi.org/10.1002/ppsc.201400217.

(62) Hermanson, G. T. *Bioconjugate Techniques*, 2nd edition.; Academic Press: San Diego, 2008.

(63) Arriortua, O. K.; Insausti, M.; Lezama, L.; Gil de Muro, I.; Garaio, E.; de la Fuente, J. M.; Fratila, R. M.; Morales, M. P.; Costa, R.; Eceiza, M.; Sagartzazu-Aizpurua, M.; Aizpurua, J. M. RGD-Functionalized Fe3O4 Nanoparticles for Magnetic Hyperthermia. *Colloids and Surfaces B: Biointerfaces* **2018**, *165*, 315–324. https://doi.org/10.1016/j.colsurfb.2018.02.031.

(64) Han, R.; Liu, Q.; Lu, Y.; Peng, J.; Pan, M.; Wang, G.; Chen, W.; Xiao, Y.; Yang, C.; Qian, Z. Tumor Microenvironment-Responsive Ag2S-PAsp(DOX)-CRGD Nanoparticles-Mediated Photochemotherapy Enhances the Immune Response to Tumor Therapy. *Biomaterials* **2022**, *281*, 121328. https://doi.org/10.1016/j.biomaterials.2021.121328.

(65) Wang, Y.; Tong, L.; Wang, J.; Luo, J.; Tang, J.; Zhong, L.; Xiao, Q.; Niu, W.; Li, J.; Zhu, J.; Chen, H.; Li, X.; Wang, Y. CRGD-Functionalized Nanoparticles for Combination Therapy of Anti-Endothelium Dependent Vessels and Anti-Vasculogenic Mimicry to Inhibit the Proliferation of Ovarian Cancer. *Acta Biomaterialia* **2019**, *94*, 495–504. https://doi.org/10.1016/j.actbio.2019.06.039.

(66) Richard, S.; Boucher, M.; Lalatonne, Y.; Mériaux, S.; Motte, L. Iron Oxide Nanoparticle Surface Decorated with CRGD Peptides for Magnetic Resonance Imaging of Brain Tumors. *Biochimica et Biophysica Acta (BBA) - General Subjects* **2017**, *1861* (6), 1515–1520. https://doi.org/10.1016/j.bbagen.2016.12.020.

(67) Bolley, J.; Lalatonne, Y.; Haddad, O.; Letourneur, D.; Soussan, M.; Pérard-Viret, J.; Motte, L. Optimized Multimodal Nanoplatforms for Targeting Avβ3 Integrins. *Nanoscale* **2013**, *5* (23), 11478–11489. https://doi.org/10.1039/C3NR03763K.

(68) Bolley, J.; Guenin, E.; Lievre, N.; Lecouvey, M.; Soussan, M.; Lalatonne, Y.; Motte, L. Carbodiimide versus Click Chemistry for Nanoparticle Surface Functionalization: A Comparative Study for the Elaboration of Multimodal Superparamagnetic Nanoparticles Targeting $\alpha_v \beta_3$ Integrins. *Langmuir* **2013**, *29* (47), 14639–14647. https://doi.org/10.1021/la403245h.

(69) Panahifar, A.; Mahmoudi, M.; Doschak, M. R. Synthesis and in Vitro Evaluation of Bone-Seeking Superparamagnetic Iron Oxide Nanoparticles as Contrast Agents for Imaging Bone Metabolic Activity. *ACS Appl. Mater. Interfaces* **2013**, *5* (11), 5219–5226. https://doi.org/10.1021/am4010495.

(70) Perton, F.; Tasso, M.; Muñoz Medina, G. A.; Ménard, M.; Blanco-Andujar, C.; Portiansky, E.; van Raap, M. B. F.; Bégin, D.; Meyer, F.; Begin-Colin, S.; Mertz, D. Fluorescent and Magnetic Stellate Mesoporous Silica for Bimodal Imaging and Magnetic Hyperthermia. *Applied Materials Today* **2019**, *16*, 301–314. https://doi.org/10.1016/j.apmt.2019.06.006.

(71) Sun, E. Y.; Josephson, L.; Weissleder, R. “Clickable” Nanoparticles for Targeted Imaging. *Mol Imaging* **2006**, *5* (2), 7290.2006.00013. https://doi.org/10.2310/7290.2006.00013.

(72) Bartczak, D.; Kanaras, A. G. Preparation of Peptide-Functionalized Gold Nanoparticles Using One Pot EDC/Sulfo-NHS Coupling. *Langmuir* **2011**, *27* (16), 10119–10123. https://doi.org/10.1021/la2022177.

(73) Jia, H.; Zhang, Y.; Guo, Q.; Zeng, X.; Yuan, Y.; Wang, Z.; Gao, Z.; Yue, T. Epsilon-Polylysine Based Magnetic Nanospheres as an Efficient and Recyclable Antibacterial Agent for Alicyclobacillus Acidoterrestris. *Food Chemistry* **2021**, *364*, 130382. https://doi.org/10.1016/j.foodchem.2021.130382.

(74) Moradi, N.; Muhammadnejad, S.; Delavari, H.; Pournoori, N.; Oghabian, M. A.; Ghafouri, H. Bio-Conjugation of Anti-Human CD3 Monoclonal Antibodies to Magnetic Nanoparticles by Using Cyanogen Bromide: A Potential for Cell Sorting and Noninvasive Diagnosis. *International Journal of Biological Macromolecules* **2021**, *192*, 72–81. https://doi.org/10.1016/j.ijbiomac.2021.09.129.

(75) Han, D.; Zhang, B.; Chong, C.; Rong, C.; Tan, J.; Yang, R. A Strategy for Iron Oxide Nanoparticles to Adhere to the Neuronal Membrane in the Substantia Nigra of Mice. *J. Mater. Chem. B* **2020**, *8* (4), 758–766. https://doi.org/10.1039/C9TB02066G.

(76) Saha, A.; Ben Halima, H.; Saini, A.; Gallardo-Gonzalez, J.; Zine, N.; Viñas, C.; Elaissari, A.; Errachid, A.; Teixidor, F. Magnetic Nanoparticles Fishing for Biomarkers in Artificial Saliva. *Molecules* **2020**, *25* (17), 3968. https://doi.org/10.3390/molecules25173968.

(77) Wen, Y.; Xu, M.; Liu, X.; Jin, X.; Kang, J.; Xu, D.; Sang, H.; Gao, P.; Chen, X.; Zhao, L. Magnetofluorescent Nanohybrid Comprising Polyglycerol Grafted Carbon Dots and Iron Oxides: Colloidal Synthesis and Applications in Cellular Imaging and Magnetically Enhanced Drug Delivery. *Colloids and Surfaces B: Biointerfaces* **2019**, *173*, 842–850. https://doi.org/10.1016/j.colsurfb.2018.10.073.

(78) Totaro, K. A.; Liao, X.; Bhattacharya, K.; Finneman, J. I.; Sperry, J. B.; Massa, M. A.; Thorn, J.; Ho, S. V.; Pentelute, B. L. Systematic Investigation of EDC/SNHS-Mediated Bioconjugation Reactions for Carboxylated Peptide Substrates. *Bioconjugate Chem.* **2016**, *27* (4), 994–1004. https://doi.org/10.1021/acs.bioconjchem.6b00043.

(79) Lee, H.-Y.; Li, Z.; Chen, K.; Hsu, A. R.; Xu, C.; Xie, J.; Sun, S.; Chen, X. PET/MRI Dual-Modality Tumor Imaging Using Arginine-Glycine-Aspartic (RGD)–Conjugated Radiolabeled Iron Oxide Nanoparticles. *J Nucl Med* **2008**, *49* (8), 1371–1379. https://doi.org/10.2967/jnumed.108.051243.

(80) Tasso, M.; Pons, T.; Lequeux, N.; Nguyen, J.; Lenkei, Z.; Zala, D. NanoPaint: A Tool for Rapid and Dynamic Imaging of Membrane Structural Plasticity at the Nanoscale. *Small* **2019**, *15* (47), 1902796. https://doi.org/10.1002/smll.201902796.

(81) Liu, Z.-Y.; Yan, G.-H.; Li, X.-Y.; Zhang, Z.; Guo, Y.-Z.; Xu, K.-X.; Quan, J.-S.; Jin, G.-Y. GE11 Peptide Modified CSO-SPION Micelles for MRI Diagnosis of Targeted Hepatic Carcinoma. *Biotechnology & Biotechnological Equipment* **2021**, *35* (1), 1574–1586. https://doi.org/10.1080/13102818.2021.1997154.

(82) Yang, C.; Mi, X.; Su, H.; Yang, J.; Gu, Y.; Zhang, L.; Sun, W.; Liang, X.; Zhang, C. GE11-PDA-Pt@USPIOs Nano-Formulation for Relief of Tumor Hypoxia and MRI/PAI-Guided Tumor Radio-Chemotherapy. *Biomater. Sci.* **2019**, *7* (5), 2076–2090. https://doi.org/10.1039/C8BM01492B.

Credit author statements

Barbara Freis: Co-writing- Original draft preparation, nanoparticles synthesis, dendronization and P22 coupling investigations, vizualization

María De Los Ángeles Ramírez: co-writing- Original draft preparation, cell studies investigations

Sonia Furgiuele: cell studies validation

Fabrice Journe: P22 choice and cells validation

Clémence Cheignon: HPLC-UV methodology

Loïc J. Charbonnière: HPLC-UV conceptualization

Céline Henoumont: HRMAS NMR conceptualization and methodology

Celine Kiefer: Ressources and nanoparticles investigation

Damien Mertz: Validation

Christine Affolter-Zbaraszczuk: cells studies methodology and ressources

Florent Meyer: cells studies validation

Sven Saussez: head and Neck cancer methodology

Sophie Laurent: conceptualization, funding acquisition, co-project administration, co-supervision

Mariana Tasso: Cell cytotoxicity and cell internalization conceptualization, peptide coupling conceptualization, cells studies investigations, validation

Sylvie Bégin-Colin: conceptualization, funding acquisition, co-project administration, co-supervision, writing and review

GA

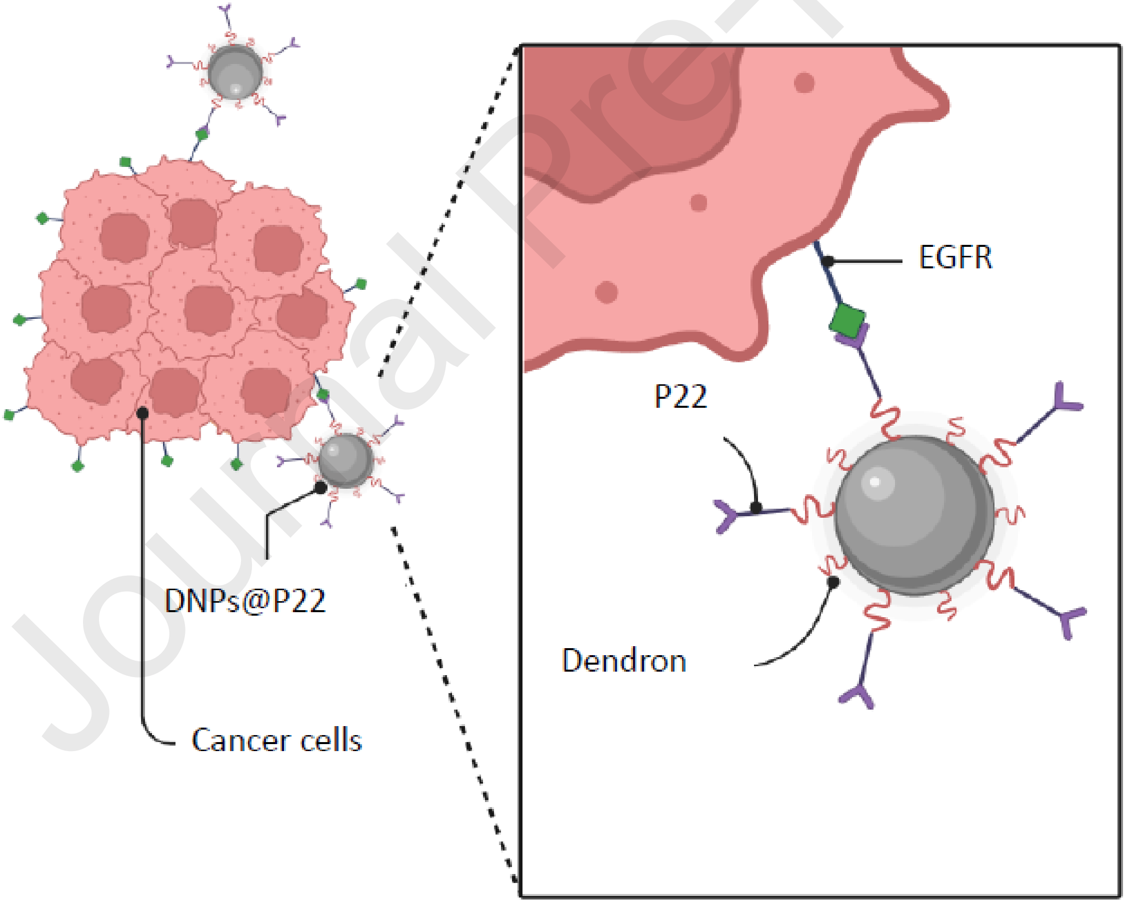

Figures in paper :
Figure 1

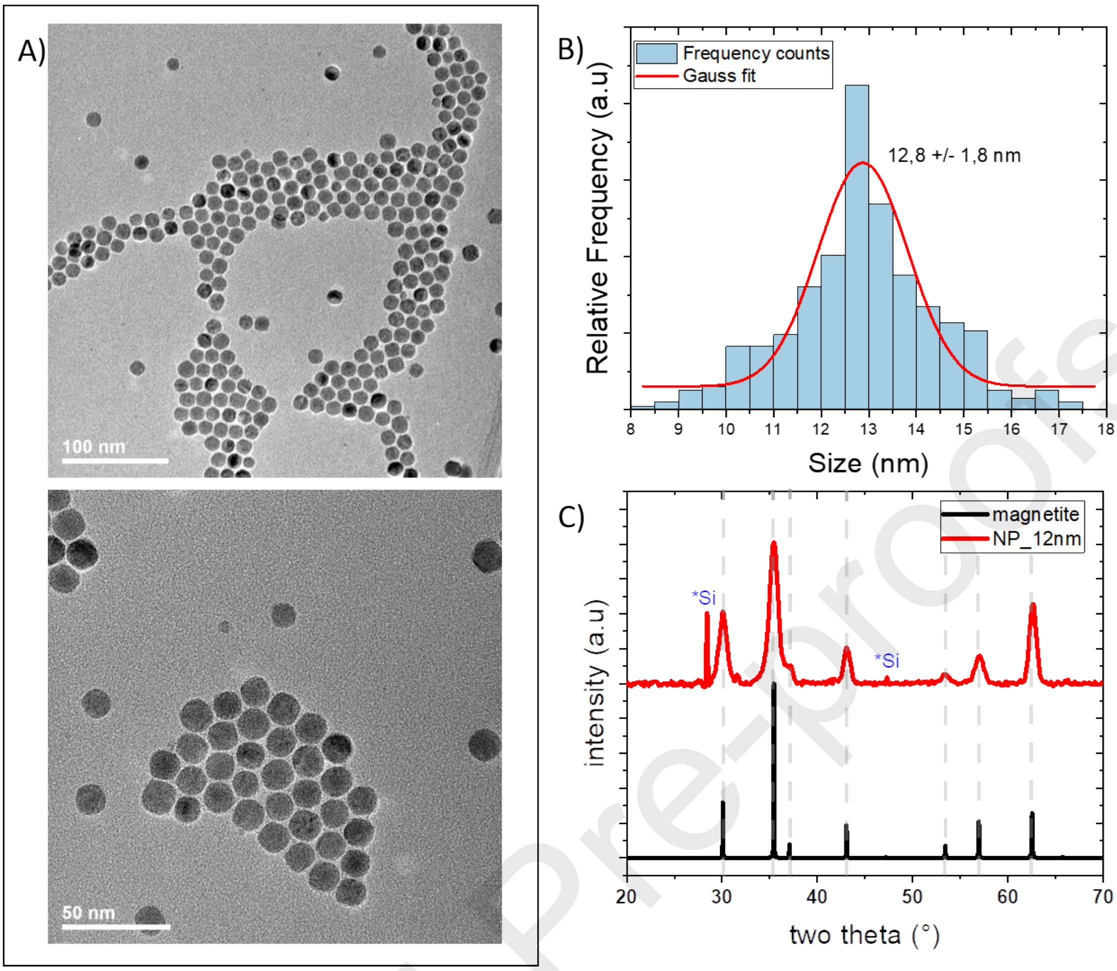

*Figure 1: A) TEM images of IONPs, B) size distribution determined from TEM images, and C) theoretical magnetite and IONPs XRD pattern (*Si is an internal reference).*

Figure 2

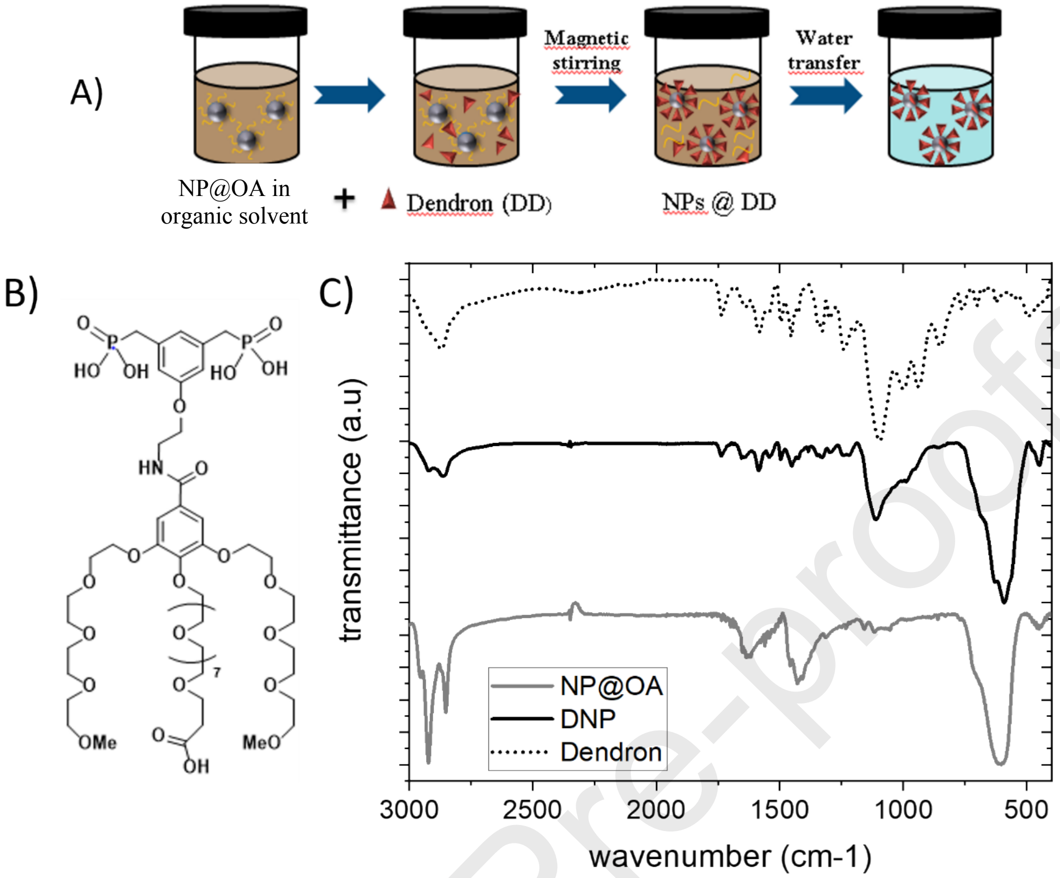

Figure 2: A) Scheme of the ligand exchange process B) Scheme of the dendron molecule, C) FTIR spectra of the dendron (black doted spectrum), of IONPs coated with oleic acid (grey spectrum) and of DNPs (black spectrum).

Figure 3

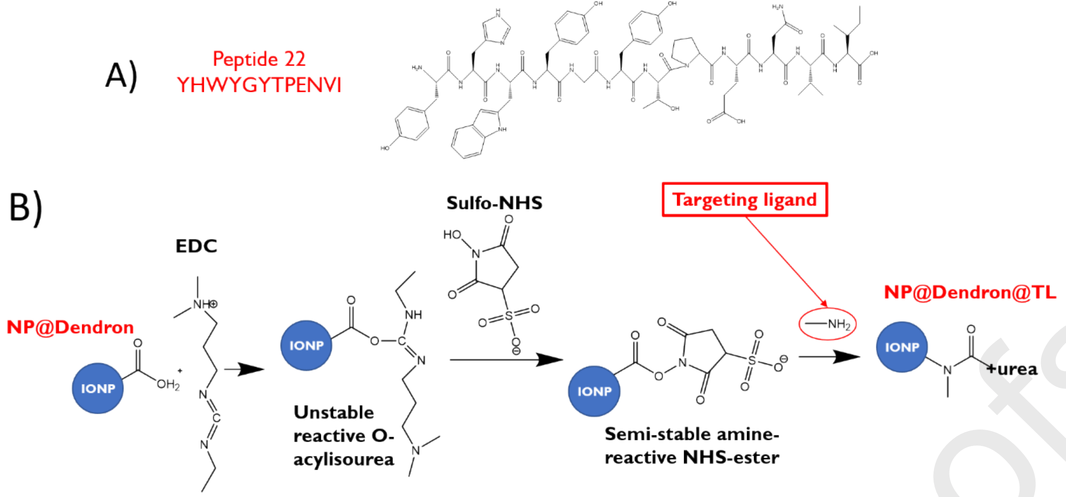

Figure 3 : A) Chemical structure of P22 B) Carbodiimation reaction: first step: activation of the carboxylate groups at the DNP surface. Second step: amide bond formation between the active carboxylates and primary P22 amine groups.

Figure 4

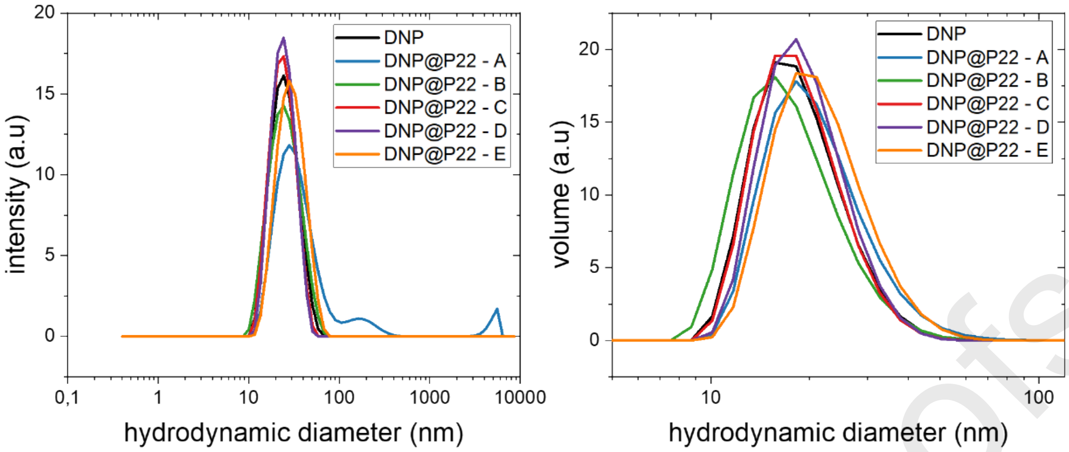

Figure 4: Mean hydrodynamic size distribution measured by DLS after the coupling reactions for the different protocols (A-E) with 0.6 molar equivalent of P22 compared to the carboxylate groups present on the dendron molecule. A) Hydrodynamic size distribution in intensity, B) Hydrodynamic size distribution in volume.

Figure 5

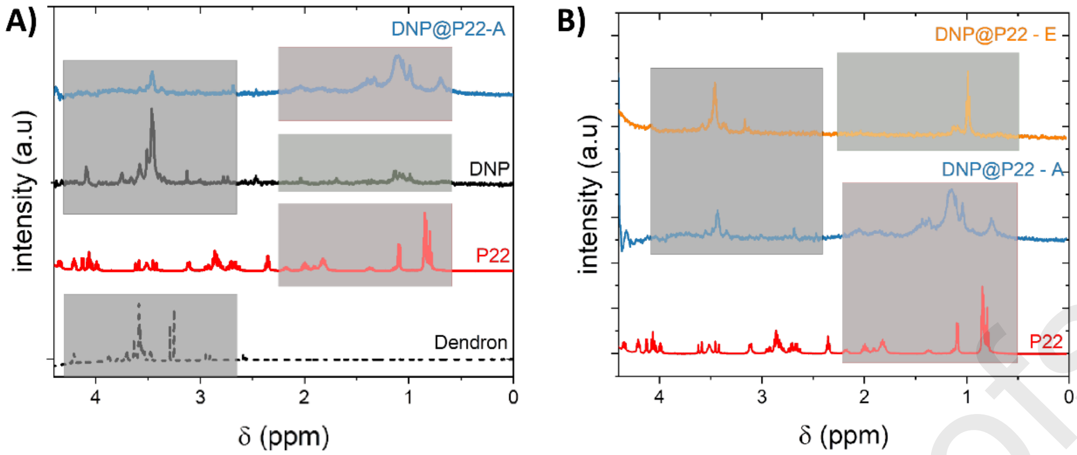

Figure 5: A) comparison of HRMAS spectra of (from top to bottom): DNP@P22-A (blue), DNP (black), P22 (red) and dendron (black dots), B) Comparison of HRMAS spectra of (from top to bottom): DNP@P22 – optimized protocol E (orange), DNP@P22 – A (blue) and P22 (red).

Figure 6

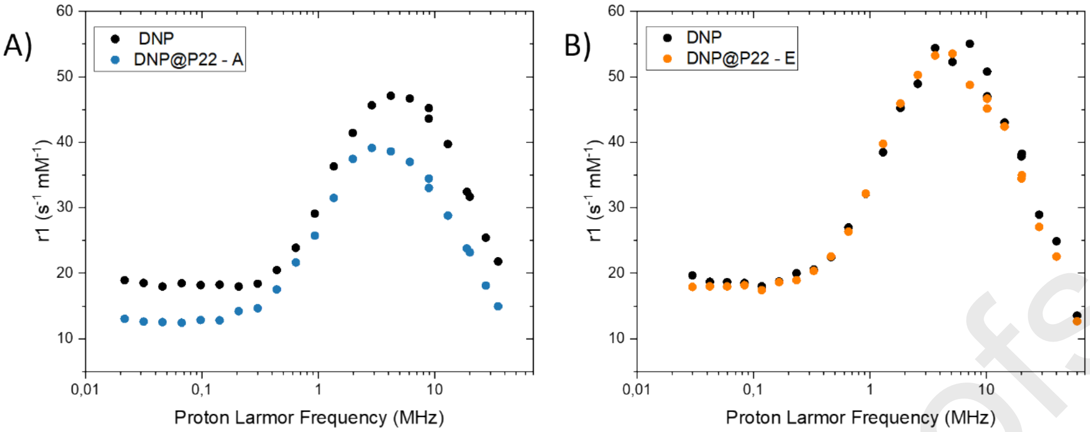

Figure 6: A) NMRD profiles of DNP (black) and DNP@P22-A (blue), B) NMRD profiles of DNP (black) and DNP@P22 -E (orange).

Figure 7

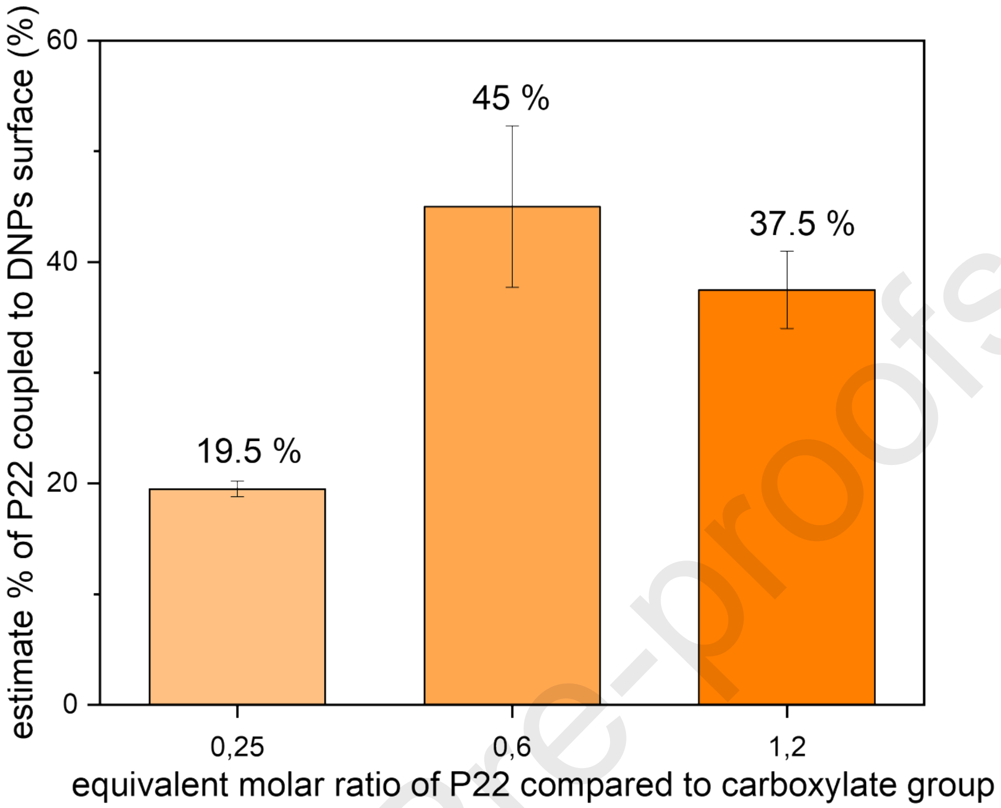

Figure 7: Estimation of P22 coupling after protocol E with 0.25, 0.6 and 1.2 equivalent of P22. The bars show the mean percentage with their respective standard deviations.

Figure 8

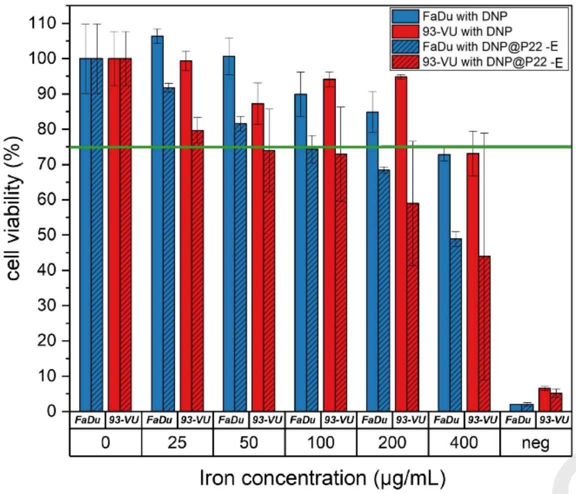

Figure 8: Cell viability of FaDu (blue) and 93-VU (red) cell monolayers as a function of the amount of DNPs and DNPS@P22–E. Neg: negative control with DMSO.

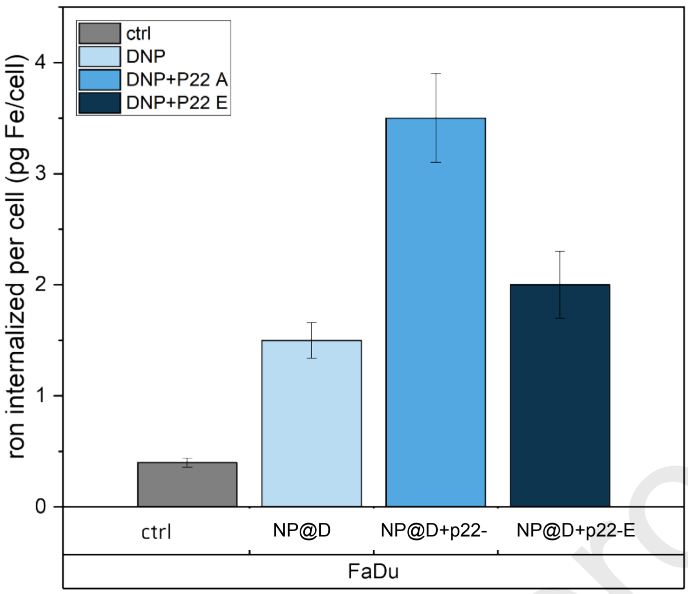

Figure 9: Amount of iron internalized in cells with DNPs and DNPs@P22 prepared with the protocol A (DNP@P22 – A) and protocol E (DNP@P22 – E) with 0.6 molar equivalent of P22 compared to carboxylate group (concentration of suspension: 100 µg Fe/mL). The test was carried out once with triplicate.

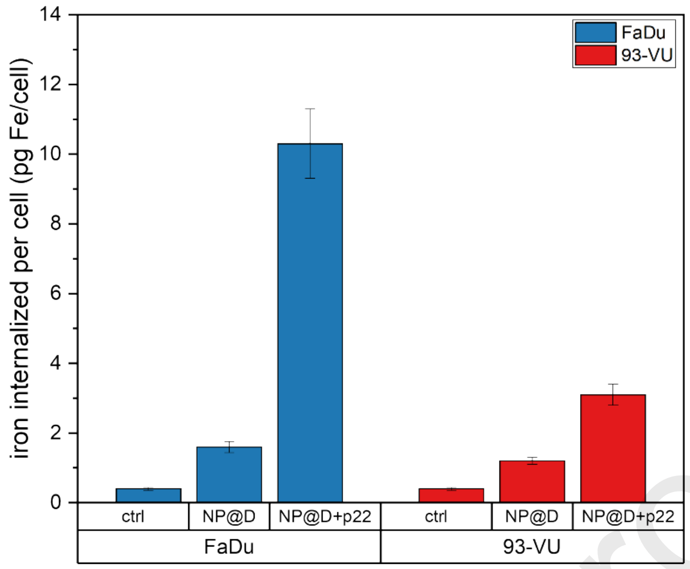

Figure 10: Amount of iron internalized by FaDu and 95-Vu cells with DNPs and DNPs@P22 prepared with the protocol E and a P22 molar equivalent of 1.2 (coverage 37.5%). NP concentration: 100 µgFe/mL).

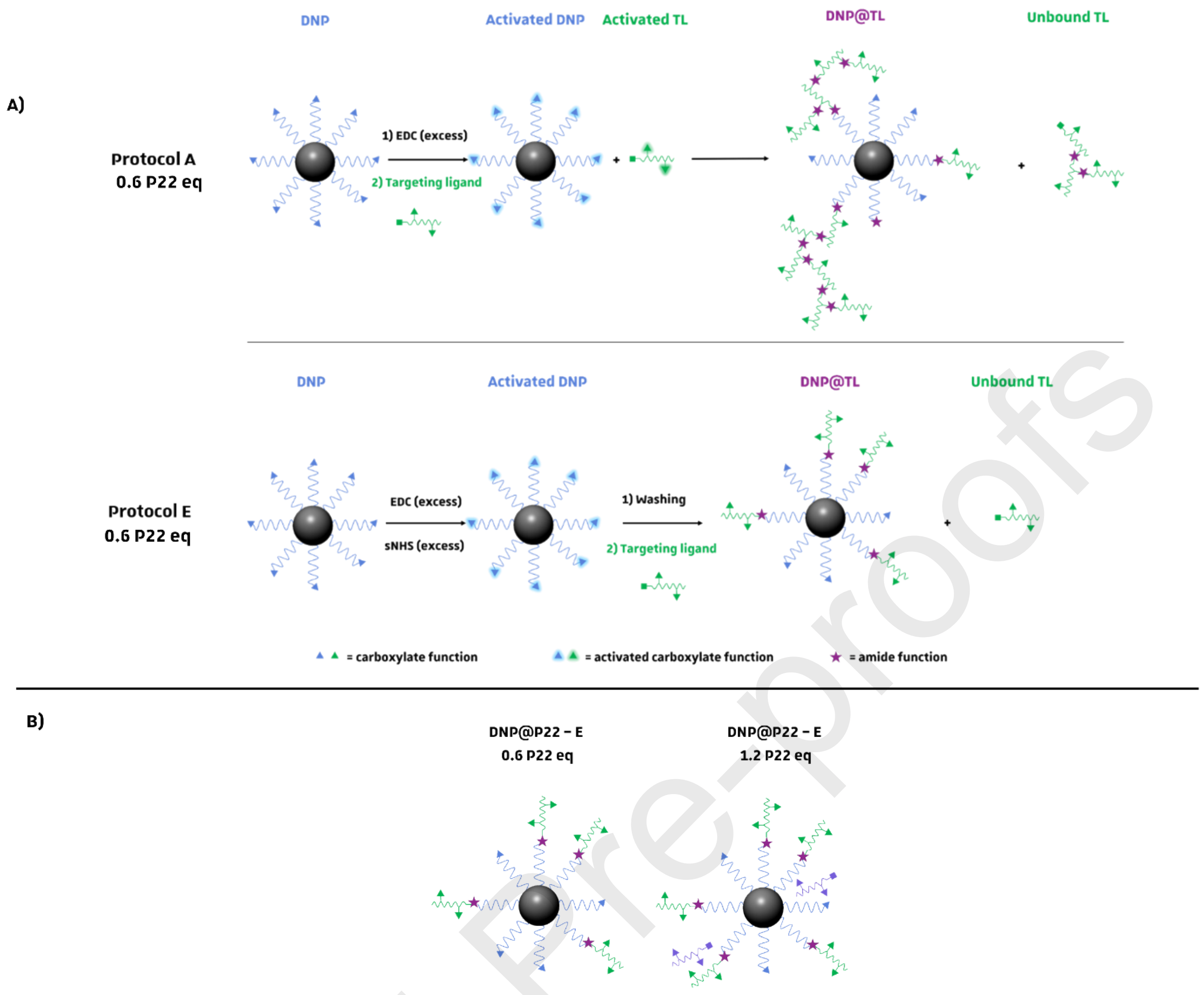

Figure 11: Hypothesis about P22 coverage to explain in vitro internalization results for A) protocols A and E with 0.6 P22 molar equivalent compared to dendron molecules and B) protocol E with either 0.6 or 1.2 P22 molar equivalent compared to dendron molecules. In protocol A, the EDC is not washed after NP activation. Therefore, it remains in solution to potentially activate carboxylate groups in the TL. In protocol E, EDC and s-NHS are removed after NP activation.

Figures in SI

Figure S1

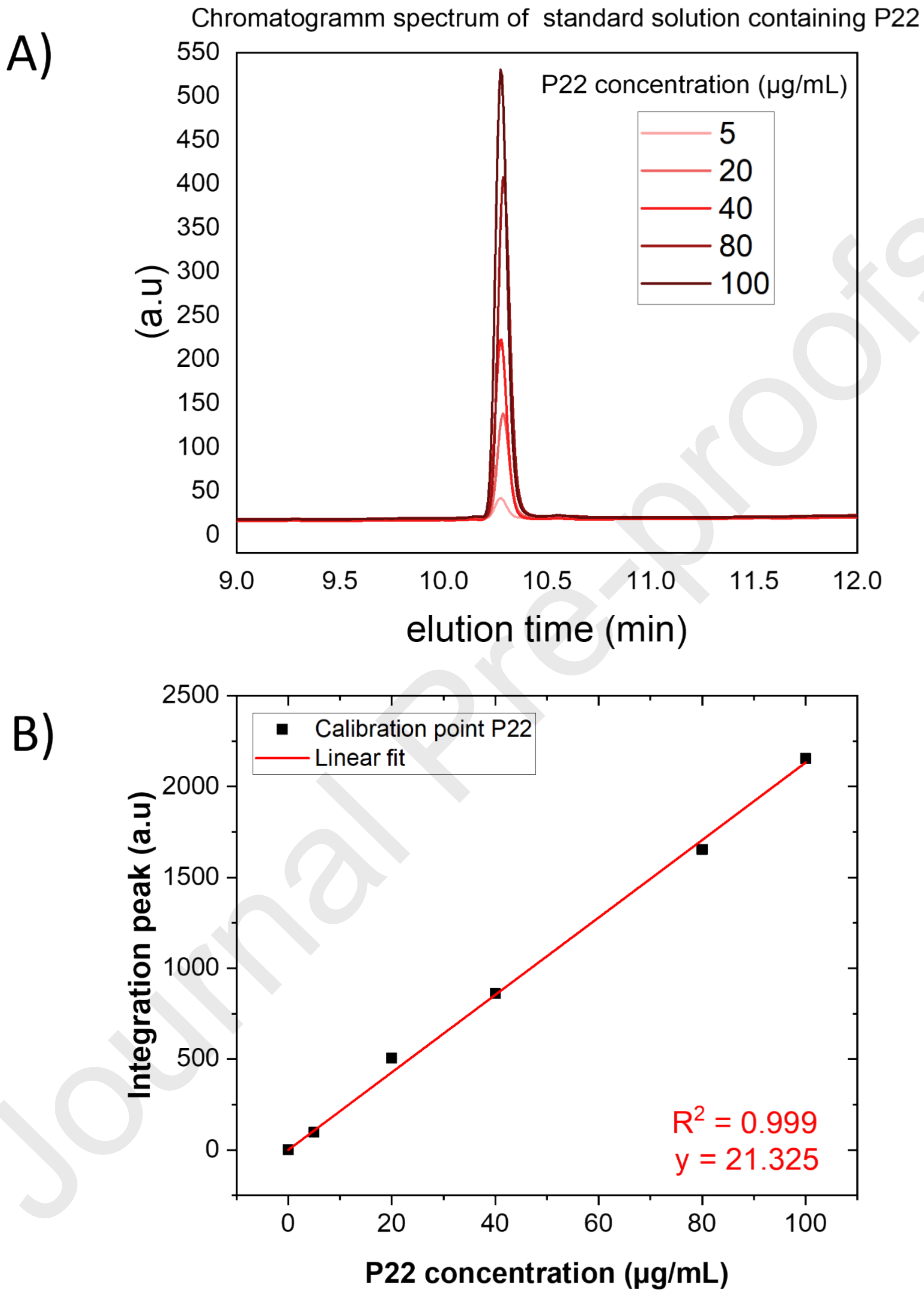

Figure S1: A) chromatograms of various standard solutions at different concentrations of P22. B) Calibration curve made at 220 nm to evaluate P22 amount on DNPs.

Figure S2

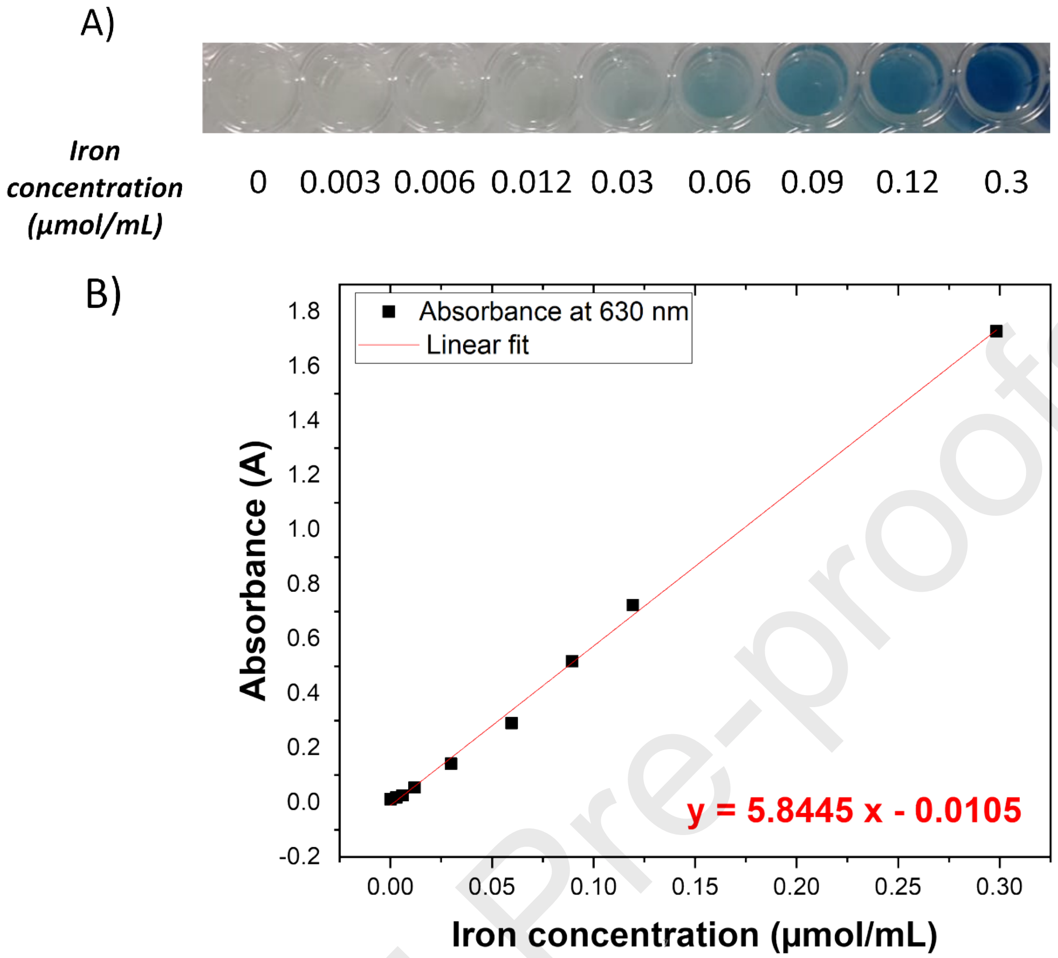

Figure S2: A) Photo of the plate obtained after reaction between the suspension of DNPs at various concentrations and the potassium ferrocyanate salt. B) Calibration curve made at 630nm to evaluate iron amount per cell.

Figure S3

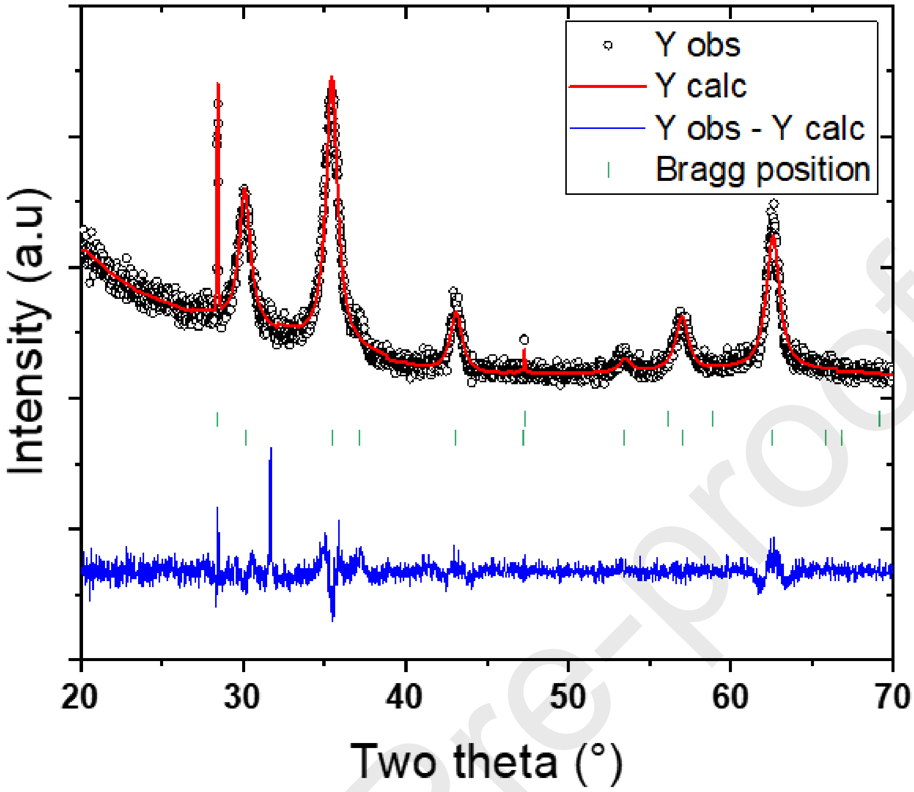

Figure S3: Raw XRD pattern (in black), refined XRD pattern (in red) after FullProf matching profile compared to Bragg position of Silica (green Dash first upper row) and magnetite (green dash, lower raw). The blue curve is the discrepancy between the raw XRD data and the refined XRD pattern.

Figure S4

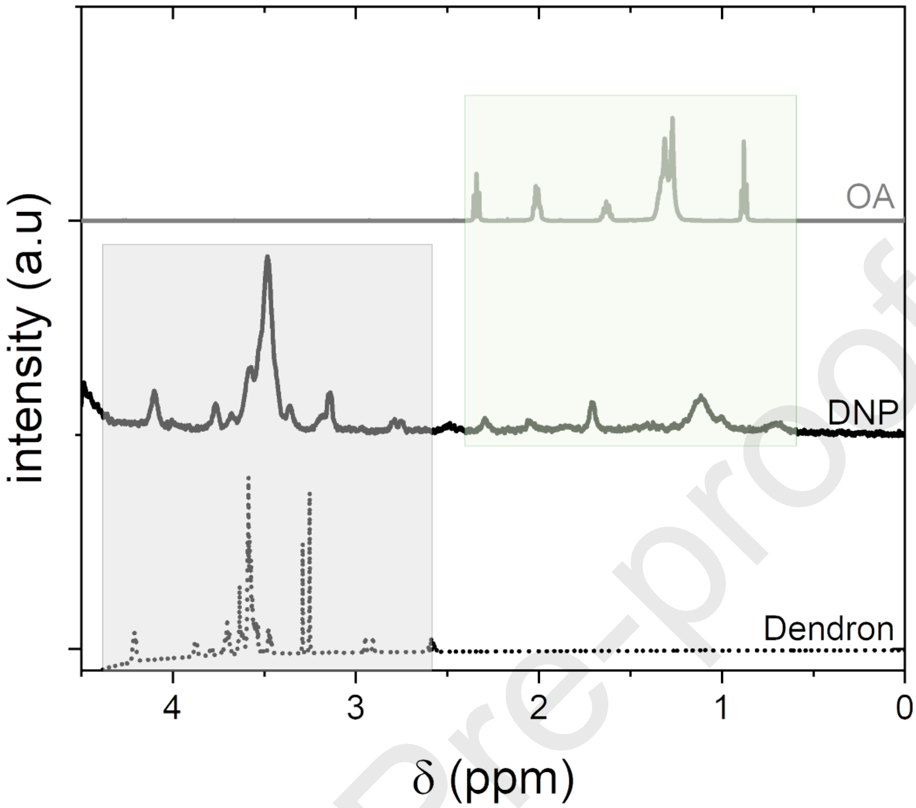

Figure S4: Comparison of HR-MAS spectrum of the dendron (black dots), the DNPs (in black) and oleic acid (in grey) showing traces of oleic acid after the ligand exchange.

Figure S5

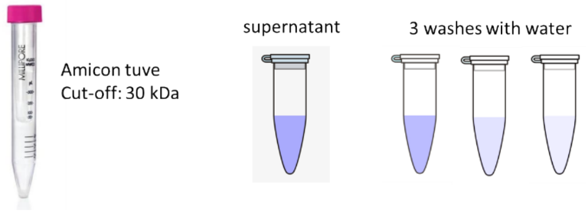

Figure S5: Indirect P22 quantification. After the coupling reactions, DNPs@P22 are separated from the reaction mixture with an amicon filter tube with a cut-off of 30 kDa. The first recovered suspension is the supernatant. Thereafter, three washes with MilliQ water followed and give rise to the washing suspensions.

Figure S6

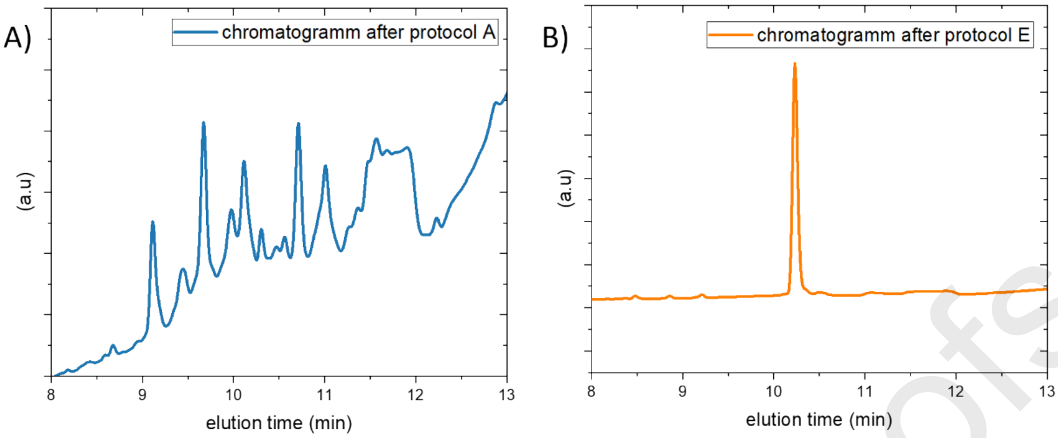

Figure S6. Comparison of chromatograms obtained after coupling p22 to the DNPs according to protocol A (A) and protocol E (B) showing several peaks in washes from protocol A.

Declaration of interests

☒ The authors declare that they have no known competing financial interests or personal relationships that could have appeared to influence the work reported in this paper.

☐ The authors declare the following financial interests/personal relationships which may be considered as potential competing interests: